Title

The Modeling and Production of Coherent Transition Radiation from Ultrashort Electron Beams

ISBN

9798190929263

Author

Azcoitia, Gia

Publication Date

2026-09-11

Peer reviewed|Thesis/dissertation

UNIVERSITY OF CALIFORNIA

Los Angeles

The Modeling and Production of Coherent Transition Radiation from Ultrashort Electron Beams

A thesis submitted in partial satisfaction of the
requirements for the degree Master of Science
in Electrical Engineering

by

Gia Azcoitia

2026

ABSTRACT OF THE THESIS

The Modeling and Production of Coherent Transition Radiation from Ultrashort Electron Beams

by

Gia Azcoitia

Master of Science in Electrical Engineering

University of California, Los Angeles, 2026

Professor Sergio Carbajo, Chair

Coherent transition radiation (CTR) provides a powerful link between the spatiotemporal structure of charged-particle beams and the emitted electromagnetic fields, underpinning a wide range of beam diagnostics and radiation sources. Despite their long-standing theoretical foundations, existing CTR frameworks have historically been restricted to simplified beam and boundary geometries. We introduce a unified, first-principles CTR framework applicable to arbitrary three-dimensional electron bunches. Beginning with the classical Ginzburg-Frank formulation, we develop a systematic and instructional description of coherent emission in terms of the bunch form factor, establishing it as the central quantity governing spectral and angular radiation characteristics. We further present a general numerical pipeline that enables the computation of CTR spectra from arbitrarily structured electron beams beyond the conventional Gaussian form factor, and provide examples of hollow Gaussian and Airy-like electron beam distributions. By extending CTR theory to arbitrarily structured

charged-particle beams, this work establishes a new, generalizable foundation for interpreting experimental measurements, designing next-generation beam diagnostics, and exploring previously inaccessible regimes of structured, broadband radiation sources.

In addition to this theoretical and computational work, experimental production and measurement of coherent transition radiation at the ARES accelerator at DESY were conducted. CTR was generated from strongly compressed, 120 MeV electron bunches using a silver radiator oriented at 45 degrees to the electron trajectory, and wavelength-resolved radiation was measured over approximately 200–1100 nm. Measurements performed at TWS2 phases of 32, 33, and 34 degrees were compared with Gaussian CTR spectra generated using the computational framework developed in this thesis. The resulting spectral fits correspond to characteristic RMS bunch durations of approximately 1.22–1.26 fs. The model additionally predicts the onset of coherence-dominated emission near 550 nm, consistent with the experimentally observed transition to quadratic charge scaling. Together, the numerical and experimental results demonstrate the use of CTR as both a source of broadband coherent radiation and a diagnostic of ultrashort electron-bunch structure.

The thesis of Gia Azcoitia is approved.

Chandrashekhar Janardan Joshi

Jia Ming Liu

James Rosenzweig

Sergio Carbajo, Committee Chair

University of California, Los Angeles

2026

Dedication

This thesis is dedicated to my grandmother, Joregelina Azcoitia, and my sister, Alex Azcoitia, who have supported me and stood by me throughout the past two years. Gracias por esperarme. Las quiero mucho.

Contents

Dedication **v**

Acknowledgments **xiv**

1 Introduction **1**

2 Theory of Coherent Transition Radiation **4**

2.1 From Transition Radiation to Coherence 4

2.2 Bunch Form Factor 5

2.2.1 Beam Structure 6

2.3 Effects of Geometry 7

3 Generalized Computational Framework for Coherent Transition Radiation **10**

3.1 From Charge Density to Radiation Observables 10

3.2 Incorporation of Tilted Interface Phase Matching 11

3.3 Evaluation for Structured Electron Beams 13

3.4 Extraction of Experimentally Relevant Observables 14

3.4.1 Three-Dimensional Gaussian Electron Beams 15

3.4.2 Longitudinally Incoherent and Coherent Regimes 16

3.4.3 Coherence Roll-Off ($\tau = 5\,\mathrm{fs}$) 18

3.5 Three-Dimensional Hollow Gaussian Electron Beams 19

3.5.1 Radial-Order Dependence of the Angular Pattern 23

3.6 Three-Dimensional Airy Electron Beams 25
3.6.1 Spectral Response of Airy Bunches with Varying Propagation Lengths and Apodization 26
3.7 Longitudinal Coherence 29
3.8 A Unifying Observation 32

4 Experimental Application: Coherent Transition Radiation from Single-Digit-Femtosecond Electron Beam Structure 34

4.1 Experimental Motivation and Overview 34
4.2 Experimental Production of CTR at ARES 35
4.3 Application of Computational Framework to Experimental Observables . . . 36

5 Conclusion 40

Bibliography 43

List of Figures

2.1 Single-electron transition-radiation angular distribution for electron kinetic energies of 5, 10, 50, and 100 MeV. The horizontal axis is the observation angle θ in radians, and the vertical axis is the single-electron spectral-angular radiation quantity W_1 in $J/(Hz \cdot Sr)$. The left panel displays W_1 on a linear vertical scale, while the right panel displays the same quantity on a logarithmic vertical scale. 5

2.2 Schematic of coherent transition radiation production from a three-dimensional electron bunch incident on a finite radiator. The bunch dimensions are characterized by σ_x, σ_y, and σ_z, the radiator size by a, and the emitted radiation direction by the polar and azimuthal observation angles θ and ϕ. The emitted bunch radiation is denoted W_n. 7

2.3 Comparison of the single-electron transition-radiation angular distribution W_1 for normal and 45° tilted interfaces at a beam energy of 100 MeV and $\phi = 0$. The horizontal axis is the observation angle θ in radians, and the vertical axis is W_1 in $J/(Hz \cdot Sr)$ on a linear scale. The normal-interface distribution is centered near $\phi = 0$, whereas tilting the interface redirects the dominant emission toward $\theta = 0.79$rad. 9

3.1 Normalized transverse electron density of a Gaussian bunch with $\sigma_x = \sigma_y = 100\,\mu$m. The horizontal and vertical axes are the transverse coordinates x and y in micrometers. Color represents the transverse density normalized to its peak value, $\rho_T/\max(\rho_T)$, so the displayed range is 0–1. 16

3.2 Spectral-angular CTR distribution W_n for a Gaussian electron bunch with $\tau = 1\,$ns (left) and $\tau = 1\,$fs (right). The horizontal axis is the observation angle θ in radians, and the vertical axis is wavelength λ in micrometers, sampled linearly from 1 to 10 μm. The plotted quantity is W_n evaluated at $\omega = \frac{2\pi c}{\lambda}$ and reported in $J/(Hz \cdot Sr)$; color is displayed using logarithmic normalization (LogNorm), not peak normalization of W_n. The two panels use independent color limits. 18

3.3 Spectral-angular CTR distribution W_n for a Gaussian electron bunch with $\tau = 5\,$fs. The horizontal axis is the observation angle θ in radians, and the vertical axis is wavelength λ in micrometers, linearly sampled from 1 to 10 μm. W_n is evaluated at $\omega = \frac{2\pi c}{\lambda}$ and displayed in $J/(Hz \cdot Sr)$ using logarithmic color normalization; the radiation values are not peak normalized. The wavelength-dependent narrowing illustrates the coherence roll-off and the preferential emission near the phase-matched direction $\theta \approx 0.79\,$rad. 19

3.4 Normalized transverse electron-density distributions for hollow Gaussian bunches with radial-order parameters $p = 0$, 1, 2, and 3 and $\sigma_x = \sigma_y = 100\,\mu$m. The horizontal and vertical axes are x and y in micrometers. Each distribution is independently peak-normalized to unity, while all panels use the common displayed color range of 0–1. Consequently, the colors compare spatial shapes rather than absolute electron densities across orders. Increasing p moves the maximum density outward and produces an increasingly large annular region. 22

3.5 Spectral-angular CTR distributions W_n from hollow Gaussian electron bunches with $p = 0$, 1, 2, and 3 and $\tau = 1\,\mathrm{fs}$. The horizontal axis is the observation angle θ in radians, and the vertical axis is wavelength λ in micrometers, linearly sampled from 1 to 10 μm. W_n is evaluated at $\omega = \frac{2\pi c}{\lambda}$ and reported in $(J/Hz \cdot Sr)$, with logarithmic color normalization and no peak normalization of the radiation intensity. All four panels use common color limits, allowing direct comparison of absolute radiation levels. Increasing p introduces additional wavelength-dependent bright and dark angular bands associated with the zeros and oscillations of the hollow-Gaussian form factor. At the same time, strong emission remains near the phase-matched direction around $\theta \approx 0.79\,\mathrm{rad}$. . . . 24

3.6 Normalized transverse electron density of the finite-energy Airy bunch at the radiator for $\sigma_x = \sigma_y = 100\,\mu\mathrm{m}$. The horizontal and vertical axes are x and y in micrometers. The plotted quantity is the real, nonnegative transverse density $\rho_T = |\psi_{Airy}|^2$, normalized to its maximum value; the color scale therefore spans 0–1. 25

3.7 Spectral-angular CTR distributions W_n for an Airy electron bunch with apodization $\alpha = 0.05$ at propagation distances $z_{prop} = 1 \times 10^7, 5 \times 10^7, 1 \times 10^8$ and 5×10^8 m corresponding to normalized propagation coordinates $\xi = 2.0, 9.8, 19.6,$ and 98.2, respectively. The horizontal axis is the observation angle θ in radians, and the vertical axis is wavelength λ in micrometers, linearly sampled from 1 to 10 μm. W_n is evaluated at $\omega = \frac{2\pi c}{\lambda}$ and displayed in $J/(Hz \cdot Sr)$ with logarithmic color normalization. The panels use common color limits and are not individually peak-normalized, permitting direct intensity comparison. Increasing propagation distance substantially changes the fine spectral-angular fringe structure while retaining strong emission near the phase-matched angular direction. 28

3.8 Spectral-angular CTR distributions W_n for Airy electron bunches with apodization parameters $\alpha = 0.05$ (left) and $\alpha = 1$ (right), evaluated at $z_{prop} = 1 \times 10^3$ m and $\xi = 1.96 \times 10^{-4}$. The horizontal axis is the observation angle θ in radians, and the vertical axis is wavelength λ in micrometers, linearly sampled from 1 to 10 μm. W_n is evaluated at $\omega = \frac{2\pi c}{\lambda}$ and reported in $J/(Hz \cdot Sr)$ using logarithmic color normalization. The two panels use the same color limits and are not independently peak-normalized. Weak apodization retains pronounced Airy interference structure, whereas stronger apodization suppresses the secondary structure and produces a smoother, Gaussian-like spectral-angular envelope. 29

3.9 Longitudinal coherence threshold for Gaussian electron bunches with $Q = 5\,\mathrm{pC}$ and RMS temporal durations $\sigma_t = 10\,\mathrm{ps}, 1\,\mathrm{ps}, 100\,\mathrm{fs}$, and $10\,\mathrm{fs}$. Each panel plots the dimensionless coherent-to-incoherent radiation ratio $\frac{W_{coh}}{W_{icoh}} = (N_e - 1)|f|^2$ versus wavelength λ in micrometers. Both axes are logarithmic. The horizontal dashed line marks $\frac{W_{coh}}{W_{incoh}} = 1$, which defines the onset of coherence, and the vertical dashed lines indicate the corresponding threshold wavelengths $\lambda_c = 4511.96, 450.88, 45.12$, and $4.51\,\mu$m. 32

4.1 Measured wavelength-resolved CTR spectra and Gaussian-model fits for TWS2 phases of 32°, 33°, and 34°. The horizontal axis is wavelength in nanometers on a linear scale, spanning approximately 200–1000 nm, and the vertical axis is detector counts on a linear scale. Colored points show the measured, background-subtracted spectra, and dashed green curves show Gaussian CTR-model fits corresponding to RMS bunch durations of 1.26 fs, 1.26 fs, and 1.22 fs for 32°, 33°, and 34°, respectively. The measured spectra were averaged over 100 consecutive electron bunches. The detector counts are not normalized, and no color scale or color limits apply [1]. 38

4.2 Predicted longitudinal coherence threshold for a Gaussian electron bunch with $\sigma_t = 1.2\,\mathrm{fs}$ and $Q = 1.75\,\mathrm{pC}$. The horizontal axis is wavelength λ in micrometers on a logarithmic scale, and the vertical axis is the dimensionless coherent-to-incoherent CTR ratio $\frac{W_{coh}}{W_{incoh}}$ on a logarithmic scale. The horizontal dashed line denotes $\frac{W_{coh}}{W_{incoh}} = 1$, and the vertical dashed line marks the predicted coherence threshold $\lambda_c = 0.55\,\mu\mathrm{m}$. The ratio is not additionally normalized, and no color scale is used. The predicted threshold coincides with the experimentally observed onset of coherence-dominated charge scaling near 550 nm. 39

List of Tables

3.1 Generalized parameter space. 15

Acknowledgments

I want to express my deepest and sincerest gratitude to my advisor, Professor Sergio Carbajo, for his guidance throughout my time at UCLA. If it were not for his patience and understanding, I would not have been able to reach this point. I am deeply grateful for the trust placed in me and the opportunities provided. I would also like to thank the members of the Quantum Light-Matter Cooperative group for their support, collaboration, and the many discussions that contributed to the development of this research. This work was supported by the U.S. Department of Energy under Award No. DE-SC0026272; the U.S. Air Force Office of Scientific Research under Award No. FA9550-23-1-0409; the U.S. National Science Foundation under Award No. 2431903; and the University of California Office of the President through the Multicampus Research Programs and Initiatives (MRPI).

Chapter 1

Introduction

Ginzburg and Frank first postulated transition radiation in 1945 [2, 3], seeking to characterize the broadband electromagnetic radiation produced as an electron traverses an inhomogeneous medium. Following this conceptualization, in 1958, Garibian demonstrated X-ray production via transition radiation [4, 5]. Furthermore, transition radiation at optical wavelengths was experimentally produced in 1959 by Goldsmith and Jelley [6]. A logical extension of these experiments was the emergence of coherent transition radiation (CTR). CTR occurs when a bunch of electrons, acting together, traverses an inhomogeneous medium, and the bunch length is shorter than or comparable to the wavelength of the emitted radiation. CTR was first experimentally demonstrated in 1991 [4, 7]. Shortly thereafter, stimulated CTR was demonstrated at the Stanford SUNSHINE facility [8]. The first experiment produced radiation in the far-infrared region. It provided direct evidence of the relationship between the dimensions of an electron bunch and the wavelength of the emitted radiation. Notably, it was discovered that electron bunches emit coherently as long as their longitudinal and transverse dimensions are smaller than or comparable to the wavelength of the emitted radiation. CTR uniquely provides a direct link between the structure of an electron bunch and its corresponding electromagnetic radiation, thereby making it an attractive scheme for producing ultrashort, tailorable broadband radiation.

Moreover, CTR emission can be directly linked to the number of electrons in a bunch. Namely, the coherent component of the radiation intensity scales quadratically with the electron count [9]. Accordingly, the radiation intensity is also governed by the form factor of the electron bunch. This form factor is defined as the Fourier transform of the bunch's spatial profile. The relevance of this form factor lies in its ability to determine which components of radiation behave coherently. As such, the form factor may be thought of as what encodes the real spatiotemporal profiles of an electron bunch into its reciprocal-space radiation observables. Tailoring this form factor can produce nontraditional radiation states and structured emission profiles.

CTR is most commonly used as a diagnostic tool in accelerator science [10]. Due to its unique ability to map longitudinal structure to emitted radiation, CTR has been used to reveal the temporal profiles of relativistic beams. This treatment was proposed by Shibata et al., coinciding with the first experiment to produce CTR, in which CTR was generated at sub-millimeter and millimeter wavelengths and analyzed for its dependence on bunch parameters [7]. Moreover, CTR interferometry has become a standard method for non-destructive bunch-length reconstruction [11, 12]. Presently, many beamlines uniquely treat CTR as both a diagnostic tool and a source [13, 14]. CTR as a source is most commonly observed in terahertz radiation, namely, for single-cycle terahertz pulse generation [15, 16]. Despite well-established demonstrations of single-band emission [13, 15, 17], a strongly coherent, spectrally continuous source remains unrealized.

Coherent (i.e., superradiant, quadratic-scaling) transition radiation has been observed across wavelengths ranging from the far-infrared [13] to the optical range, with optical emission arising from single-digit-femtosecond bunch structure [1]. While single-band demonstrations remain the norm [15, 17], a spectrally continuous, multi-octave coherent source has not yet been realized. Recent theory has sharpened this opportunity by proposing generalized superradiance [18], which considers configurations that can radiate broadband, coherent fields more efficiently than conventional single-frequency-producing bunching schemes [19].[1]. With this, a plausible path to truly multi-octave emission may be realized if such a tailored bunch structure can be produced and maintained.

Through this work, we present a unified theoretical, computational, and experimental study of coherent transition radiation from ultrashort electron beams. First, a numerical CTR framework is developed that directly maps arbitrary three-dimensional electron-bunch distributions to wavelength- and angle-resolved radiation spectra, enabling the study of Gaussian and structured electron-beam distributions. This framework is then connected to an experimental campaign at the ARES accelerator at DESY, in which optical coherent transition radiation was produced and measured from strongly compressed relativistic electron bunches [1]. The experimentally measured spectra are compared with predictions from the computational framework to infer single-digit-femtosecond longitudinal bunch structure and to examine the transition from incoherent to coherent emission. Taken together, the numerical framework and the experiment at DESY address the modeling and experimental production of CTR, respectively, and demonstrate the connection between structured charge distributions and their corresponding radiation observables.

[1]"Superradiance" in this sense refers to the aforementioned coherent, quadratic enhancement, rather than the notion of Dicke superradiance in quantum optics.

Chapter 2

Theory of Coherent Transition Radiation

2.1 From Transition Radiation to Coherence

For a single electron crossing a boundary between two media of distinct dielectric constants, the spectral-angular energy distribution is given by the Ginzburg-Frank formula:

$$W_1(\omega, \Omega) = \frac{d^2W}{d\omega d\Omega} = \frac{e^2\beta^2 \sin^2\theta}{4\pi^3\epsilon_0 c(1-\beta^2\cos^2\theta)^2}, \tag{2.1}$$

where θ is the emission angle, Ω denotes the solid angle, $\beta = \frac{v}{c}$ is the normalized electron velocity, c is the speed of light, e is the elementary charge, and ϵ_0 is the vacuum permittivity [20, 21]. This equation is valid only in the far field for radiation from an infinite, ideal conducting interface [22].

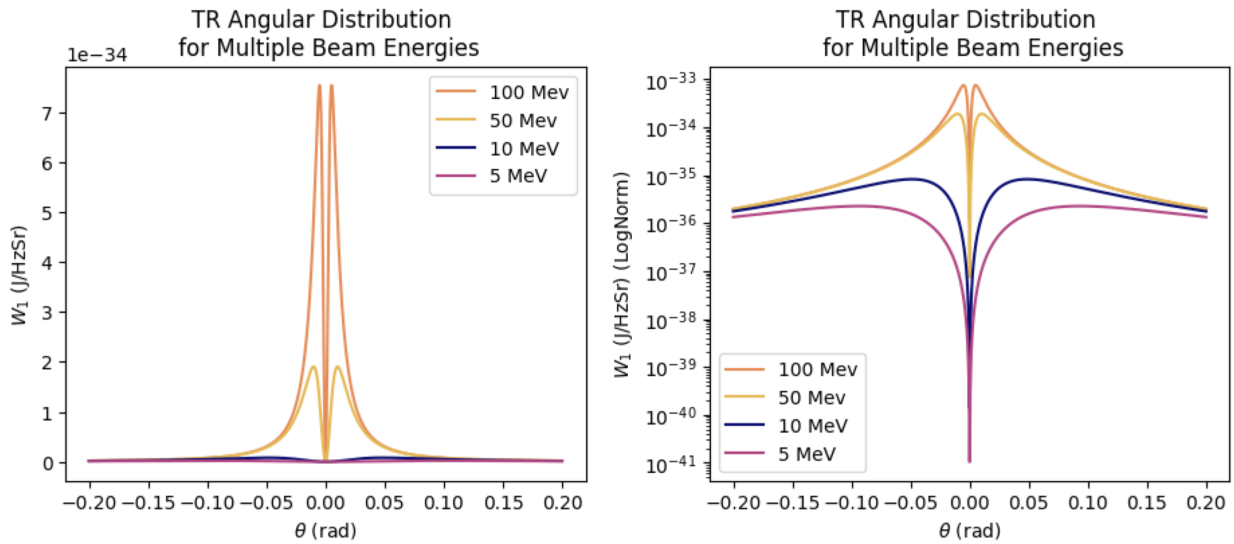

Figure 2.1: Single-electron transition-radiation angular distribution for electron kinetic energies of 5, 10, 50, and 100 MeV. The horizontal axis is the observation angle θ in radians, and the vertical axis is the single-electron spectral-angular radiation quantity W_1 in $J/(Hz \cdot Sr)$. The left panel displays W_1 on a linear vertical scale, while the right panel displays the same quantity on a logarithmic vertical scale.

When considering a bunch with N_e electrons, we see distinct features emerge as interference among electrons gives rise to coherent effects. These effects are captured by summing the individual coherent and incoherent contributions, leading to the following expression:

$$W_n(\omega, \Omega) = W_1(\omega, \Omega)[N_e + N_e(N_e - 1)|f(\bar{k})|^2], \tag{2.2}$$

where W_1 is the single-electron transition radiation and $|f(\bar{k})|^2$ is the normalized bunch form factor. This form factor, $|f(\bar{k})|$, is the Fourier transform of the electron bunch's three-dimensional charge density [22]. Like W_1, W_n has units of $J/(Hz \cdot Sr)$

2.2 Bunch Form Factor

The bunch form factor is a central quantity when considering CTR, as it is the fundamental link between electron beam structure and emitted radiation, as well as the connection between coherent and incoherent electron field contributions:

$$f(\bar{k}) = \int \rho(\bar{r}) e^{i\bar{k}\cdot\bar{r}} d^3\bar{r} \tag{2.3}$$

where $\bar{k} = (k_x, k_y, k_z)$ is the wave vector and $\bar{r} = (x, y, z)$ denotes the spatial coordinates. Notice that (2) smoothly interpolates between incoherent emission at high frequencies or large radiation angles, where $|f(\bar{k})|^2 \to 0$, and fully coherent emission at long wavelengths, where $|f(\bar{k})|^2 \to 1$.

2.2.1 Beam Structure

Consider a three-dimensional electron beam with the following spatial distribution:

$$\rho(\bar{r}) = \rho(x, y, z) = \rho(x, y)\rho(z). \tag{2.4}$$

We may further define the spatial transverse profile of the beam as $\rho_T = \rho(x, y)$ and the spatial longitudinal profile as $\rho_L = \rho(z)$. From $\rho(\bar{r})$ we can derive the form factor, which uniquely governs coherence and spectral content. Furthermore, this dependence can be expressed explicitly for a Gaussian electron beam. That is, for a three-dimensional Gaussian beam, longitudinal and transverse form factors are expressed as:

$$f_T \sim \exp(-k\sigma_T \sin\theta)^2 \tag{2.5}$$

$$f_L \sim \exp(-k\sigma_L \cos\theta)^2 \tag{2.6}$$

with $k = \frac{2\pi}{\lambda}$. From this, σ_T is the radial beam size, while σ_L is the longitudinal beam size. Using the preceding facts, it can be concluded that when the transverse size of the beam is small, the contribution of the transverse component approaches unity. The same may be concluded for the longitudinal component. Therefore, to obtain broadband, coherent radiation, the beam size should be minimized transversely and temporally.

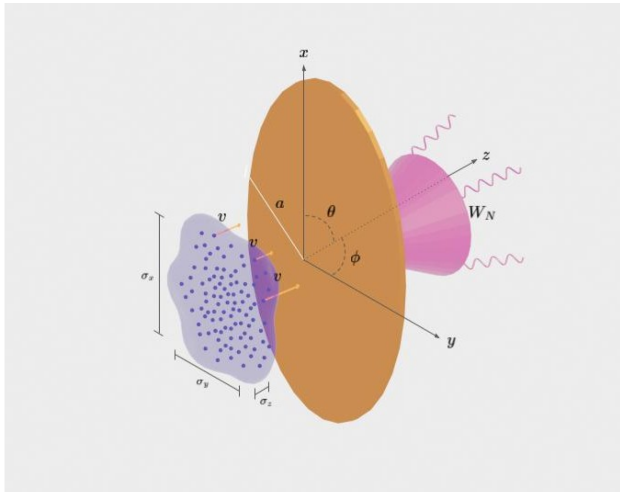

Figure 2.2: Schematic of coherent transition radiation production from a three-dimensional electron bunch incident on a finite radiator. The bunch dimensions are characterized by σ_x, σ_y, and σ_z, the radiator size by a, and the emitted radiation direction by the polar and azimuthal observation angles θ and ϕ. The emitted bunch radiation is denoted W_n.

2.3 Effects of Geometry

The behavior of the emitted radiation is contingent not only on the bunch structure but also on the physical geometry and boundary conditions. Moreover, one may begin by examining the link between radiation quality and target size. In particular, we may utilize the following formulation:

$$W_1(\omega, \Omega) = \frac{e^2 \beta^2 \sin^2\theta}{4\pi^3 \epsilon_0 c (1-\beta^2\cos^2\theta)^2}[1 - T(\omega,\theta)]^2 \tag{2.7}$$

$$T(\omega,\theta) = \frac{\omega a}{c\beta\gamma} J_0\left(\frac{\omega a \sin\theta}{c}\right) K_1\left(\frac{\omega a}{c\beta\gamma}\right) + \frac{\omega a}{c\beta^2\gamma^2\sin\theta} J_1\left(\frac{\omega a \sin\theta}{c}\right) K_0\left(\frac{\omega a}{c\beta\gamma}\right) \tag{2.8}$$

where θ is the angle of emission with respect to the axis of electron beam propagation, a is the radius of the transition radiation source, J_n is the n-th order Bessel function, and K_n is the n-th order modified Bessel function [22].

This expression encapsulates the effect of the transition radiation interface on the shape and wavelength of emitted radiation. Notably, when taking the radius of the interface, a, to infinity, we arrive at the Ginzburg-Frank formula as detailed in Eq. 1. When considering a tightly compressed bunch, both longitudinally and transversely, one may assume the target size to be large in comparison to the beam, thereby validating the original Ginzburg-Frank formulation.

The tilting of the transition radiation source also plays a significant role in the quality of the emission. Tilting the interface produces a directional enhancement in radiation [13]. In general, when considering a target tilted at ψ degrees, one may decompose the radiation from a single electron into its polarization components [23]:

$$W_1^{\parallel}(\omega, \Omega) = \frac{e^2\beta^2\cos^2\psi}{\pi^2 c}\left[\frac{\sin\theta - \beta\cos\phi\sin\psi}{(1-\beta\sin\theta\cos\phi\sin\psi)^2 - \beta^2\cos^2\theta\cos^2\psi}\right]^2 \tag{2.9}$$

$$W_1^{\perp}(\omega, \Omega) = \frac{e^2\beta^2\cos^2\psi}{\pi^2 c}\left[\frac{\beta\cos\theta\sin\phi\sin\psi}{(1-\beta\sin\theta\cos\phi\cos\psi)^2 - \beta^2\cos^2\theta\cos^2\psi}\right]^2 \tag{2.10}$$

where θ is the angle of emission with respect to the axis of electron beam propagation and ϕ is the azimuthal angle contained in the plane parallel to propagation as shown in Fig. 2.2.

We may consider these parallel and perpendicular components to compare the transition radiation produced from a normal interface and a tilted interface. Assuming a single azimuthal slice, $\phi = 0$, we can then directly compare the radiation energy distribution, W_1. Indeed, the radiation intensity produced from the tilted interface at a chosen angular slice is higher than the intensity produced from a normal interface at the same slice. This enhancement has also been demonstrated experimentally [13]. The reason for this enhancement lies in the directionality of the produced radiation. That is, when considering a normal interface, radiation will be produced collinearly with the electron and in a conical shape. Namely, radiation has been demonstrated to be concentrated around $\theta \sim \frac{1}{\gamma}$ [24]. When the interface is tilted, the surface is no longer collinear with the electron. The radiation pattern is still tied to the boundary conditions imposed by the interface, thereby causing a shift in the effective emission. As a result, an observer looking along a particular angle (for example, $\phi = 0, \theta = 45° = 0.79$ rad) may see a larger intensity.

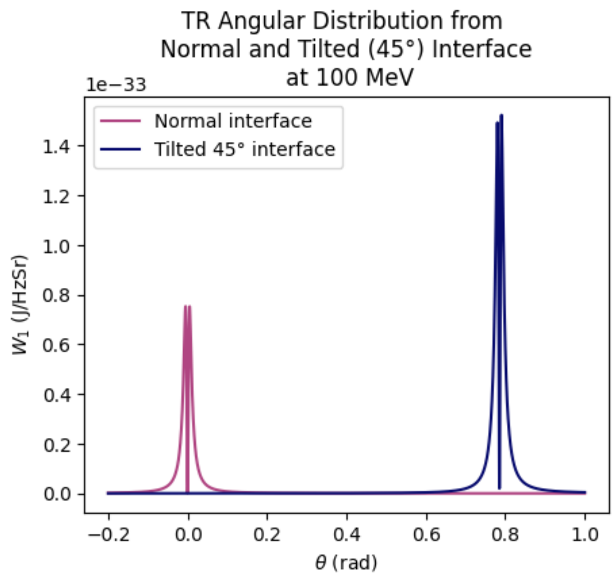

Figure 2.3: Comparison of the single-electron transition-radiation angular distribution W_1 for normal and 45° tilted interfaces at a beam energy of 100 MeV and $\phi = 0$. The horizontal axis is the observation angle θ in radians, and the vertical axis is W_1 in $J/(Hz \cdot Sr)$ on a linear scale. The normal-interface distribution is centered near $\phi = 0$, whereas tilting the interface redirects the dominant emission toward $\theta = 0.79$rad.

Chapter 3

Generalized Computational Framework for Coherent Transition Radiation

3.1 From Charge Density to Radiation Observables

To describe the transition radiation process, we first consider an electron traveling along the z axis, as detailed in Figure 3. We then generalize this to a bunch of N_e electrons to generate the spectrum of a CTR process. This simulation-based CTR scheme is implemented as a numerical model that maps a known, real, three-dimensional electron bunch distribution and relativistic beam parameters, with $\gamma >> 1$, to an angularly resolved (θ) and wavelength-resolved (λ) radiation spectrum produced from an interface with a radius of 1 mm, tilted at a 45-degree angle. The pipeline begins by defining fundamental physical constants and converting the specified beam energy into relativistic quantities. From the total electron energy, both γ and β are computed. The total charge determines the total number of electrons in the bunch, while the respective beam profiles are constructed from user-defined distributions and beam sizes. A set of candidate pulse durations is provided to explore how changes in longitudinal bunch length affect the degree of coherence in the emitted radiation.

The single-electron transition radiation spectrum is calculated using the analytical expression derived from the fields of a relativistic charge crossing a dielectric boundary, as given in Eq. 2.1 [2, 25]. The expression explicitly depends on β, γ, and θ and defines the fundamental angular envelope of the radiation. This single-electron yield $W_1(\omega, \Omega)$ represents the incoherent baseline against which a coherent enhancement of the bunch structure is later applied.

Radiation is evaluated on a two-dimensional observation grid defined by the angle θ and wavelength of emission λ. Uniform meshes in θ, λ, and ϕ are constructed. Along with this, the angular frequency is computed pointwise as $\omega = \frac{2\pi c}{\lambda}$. This grid-based formulation allows the spectral-angular radiation intensity, the bunch form factor, and the corresponding coherent enhancement to be evaluated simultaneously using array-based operations. Under this geometry, emission is azimuthally asymmetric. We therefore select a specific value of ϕ to examine, namely $\phi = 0°$.

3.2 Incorporation of Tilted Interface Phase Matching

The phase accumulation between the moving electron bunch and the emitted electromagnetic field governs longitudinal coherence in transition radiation. For an electron traveling with velocity $v = \beta c$, the conventional longitudinal phase mismatch along the electron trajectory may be expressed as:

$$\Delta k_z = \frac{\omega}{v} - \frac{\omega}{c}\cos\theta = \frac{\omega}{c}\left(\frac{1}{\beta} - \cos\theta\right). \tag{3.1}$$

The corresponding formation length is inversely proportional to the mismatch [25],

$$L_f \sim \frac{2c}{\omega(1 - \beta^2 + \theta^2)}. \tag{3.2}$$

Thus, a small longitudinal phase mismatch corresponds to a longer formation length.

For the tilted interface geometry presently considered, the form factor is evaluated using transformed Fourier coordinates. For radiation of frequency ω emitted in the direction (θ, ϕ), the transverse components of the radiation wave vector are [26]

$$k_x = \frac{\omega}{c} \sin\theta \cos\phi \tag{3.3}$$

$$k_y = \frac{\omega}{c} \sin\theta \sin\phi. \tag{3.4}$$

For an interface tilted by an angle ψ, the Fourier transform of the bunch is evaluated at

$$\Delta k_x = \frac{k_x - (\omega/v)\sin\psi}{\cos\psi} \tag{3.5}$$

$$k'_y = k_y \tag{3.6}$$

and

$$k'_z = \frac{\omega}{v}. \tag{3.7}$$

The quantity Δk_x represents the effective wave vector mismatch introduced by the tilted interface, while k'_z is the longitudinal spatial frequency associated with the moving bunch. The three-dimensional bunch form factor is therefore evaluated as $f(\bar{k}) = \tilde{\rho}(\Delta k_x, k'_y, k'_z)$. This transformation accounts for the relative arrival-time delays of electrons at different transverse positions on the tilted radiator and thus incorporates the velocity-matching condition of the interface geometry [26]. Moreover, for a 45° interface, the transformed coordinates reduce to

$$\Delta k_x = \sqrt{2} k_x - \frac{\omega}{v} \tag{3.8}$$

$$k'_y = \frac{\omega}{c} \sin\theta \sin\phi \tag{3.9}$$

and

$$k'_z = \frac{\omega}{v}. \tag{3.10}$$

These are the Fourier space coordinates used to interpolate the numerically calculated three-dimensional transform of the electron bunch charge density.

3.3 Evaluation for Structured Electron Beams

With these tools, we can now model the energy-spectral-angular density of an electron bunch. We choose to consider three families of structured beams as examples. The first and simplest distribution modeled was a three-dimensional Gaussian electron bunch.

$$\rho(x, y, z) \propto \exp\left(-\frac{x^2}{2\sigma_x^2}\right) \exp\left(-\frac{y^2}{2\sigma_y^2}\right) \exp\left(-\frac{z^2}{2\sigma_z^2}\right) \tag{3.11}$$

where the longitudinal RMS length σ_z is obtained from the temporal RMS pulse duration, τ, as $\sigma_z = c\tau$. Along with this Gaussian distribution, hollow Gaussian profiles were also simulated via the following formulation:

$$\rho(x, y, z) \propto \frac{(x^2 + y^2)^p}{\pi^{3/2}} \exp\left(-\frac{x^2}{2\sigma_x^2}\right) \exp\left(-\frac{y^2}{2\sigma_y^2}\right) \exp\left(-\frac{z^2}{2\sigma_z^2}\right). \tag{3.12}$$

Here, p is a nonnegative radial-order parameter that controls the degree of hollowness of the transverse electron distribution. The case $p = 0$ reduces to a conventional Gaussian bunch, while increasing p shifts the peak charge density outward and produces progressively larger annular profiles. Like Gaussian bunches, hollow Gaussian electron bunches are physically realizable and have been experimentally produced [27].

Lastly, Airy profiles were also modeled. Building Airy profiles using a scheme similar to that for the aforementioned profiles presented a unique challenge, as Airy distributions do not share the structure of the Gaussian beams. We take the Airy distribution as given in [28]:

$$\begin{aligned} \rho(x, y, z) \propto \operatorname{Ai}\left(\frac{x}{\sigma_x} - \frac{z}{4k^2\sigma_x^4} + i\frac{\alpha z}{k\sigma_x^2}\right) \operatorname{Ai}\left(\frac{y}{\sigma_y} - \frac{z}{4k^2\sigma_y^4} + i\frac{\alpha z}{k\sigma_y^2}\right) \\ \times \exp\left(\frac{\alpha x}{\sigma_x} - \frac{\alpha^2 z^2}{2k^2\sigma_x^4} - i\frac{z^3}{12k^3\sigma_x^6} + i\frac{\alpha^2 z}{2k\sigma_x^2} + i\frac{xz}{2k\sigma_x^2}\right) \\ \times \exp\left(\frac{\alpha y}{\sigma_y} - \frac{\alpha^2 z^2}{2k^2\sigma_y^4} - i\frac{z^3}{12k^3\sigma_y^6} + i\frac{\alpha^2 z}{2k\sigma_y^2} + i\frac{yz}{2k\sigma_y^2}\right). \end{aligned} \tag{3.13}$$

$Ai(\cdot)$ is defined in the following manner:

$$\mathrm{Ai}(x) = \frac{1}{\pi}\int_0^{\infty} \cos\left(\frac{t^3}{3} + xt\right) dt. \tag{3.14}$$

The constant $k_e = \frac{p}{\hbar} = \frac{2\pi}{\lambda_e}$ is the de Broglie wavenumber of the electrons, where λ_e is the electron's wavelength and α is the level of apodization. The normalized propagation distance is defined as $\xi = \frac{z_{prop}}{k_e \sigma_x^2}$ [28, 29].

Notably, Airy profiles have an oscillatory tail. To model the Airy profile with a finite longitudinal size, as was required when modeling coherence in Section 3.7, a Gaussian envelope is multiplied by the Airy profile, yielding [28]:

$$\begin{aligned}\rho(x,y,z) = {} & \mathrm{Ai}\left(\frac{x}{\sigma_x} - \frac{z}{4k^2\sigma_x^4} + i\frac{\alpha z}{k\sigma_x^2}\right) \mathrm{Ai}\left(\frac{y}{\sigma_y} - \frac{z}{4k^2\sigma_y^4} + i\frac{\alpha z}{k\sigma_y^2}\right) \\ & \times \exp\left(\frac{\alpha x}{\sigma_x} - \frac{\alpha^2 z^2}{2k^2\sigma_x^4} - i\frac{z^3}{12k^3\sigma_x^6} + i\frac{\alpha^2 z}{2k\sigma_x^2} + i\frac{xz}{2k\sigma_x^2}\right) \\ & \times \exp\left(\frac{\alpha y}{\sigma_y} - \frac{\alpha^2 z^2}{2k^2\sigma_y^4} - i\frac{z^3}{12k^3\sigma_y^6} + i\frac{\alpha^2 z}{2k\sigma_y^2} + i\frac{yz}{2k\sigma_y^2}\right) \exp\left(-\frac{z^2}{2\sigma_z^2}\right).\end{aligned} \tag{3.15}$$

3.4 Extraction of Experimentally Relevant Observables

Fourier transforming the charge distributions yields an approximate closed-form array for the three-dimensional form factor that simultaneously accounts for radial beam size, longitudinal bunch duration, and observation angle, as defined in (3). The pipeline evaluates such an array directly on the (θ, λ, ϕ) mesh grid. The total radiated spectrum from the bunch is computed using (2). For visualization, the resulting spectral-angular distributions are displayed as logarithmically scaled heatmaps in (θ, λ) space. Percentile-based normalization is used to ensure a consistent dynamic range across distinct pulse-duration spectra. Again, to obtain a reduced spectrum comparable to experimental measurements, ϕ is set to $0°$.

We now present three spectra generated using the described schemes to illustrate relevant physical phenomena and current code capabilities. In particular, we focus on three structured electron-bunch distributions: Gaussian, hollow Gaussian, and Airy. Moreover, the goal is not only to display representative CTR spectra but to make explicit, for each case, how the analytical structure of the form factor $|f(\bar{k})|^2$ produces particular spectral features. The parameter space common to all three cases is summarized in Table 3.1.

Table 3.1: Generalized parameter space.

Parameter	Symbol	Value
Temporal bunch length	τ	$[10^{-9}, 10^{-15}]$s
Transverse beam size	$\sigma_x = \sigma_y = \sigma_T$	10^{-4}m
Longitudinal beam size	$\sigma_z = \sigma_L$	$[3 \times 10^{-7}, 3 \times 10^{-1}]$ m
Emission wavelength	λ	$[10^{-6}, 10^{-5}]$ m
Interface radius	α	10^{-3} m
Interface tilt	a	$45^\circ = 0.79$ rad
Azimuthal observation angle	ϕ	$0^\circ = 0$ rad
Bunch charge	Q	5 pC
Kinetic beam energy	E	100 MeV
Lorentz factor	γ	235.80
Normal observation angle	θ	$[-0.0035^\circ, 0.0035^\circ] = [-0.2, 0.2]$ rad
Airy apodization	α	$0.05, 1$
Airy propagation length	z_{prop}	$[1 \times 10^3, 5 \times 10^8]$ m

3.4.1 Three-Dimensional Gaussian Electron Beams

The simplest and most well-documented electron distribution, with respect to CTR production, is the Gaussian distribution. For a three-dimensional Gaussian electron bunch, the Fourier transform of the charge density is also Gaussian. However, for an obliquely oriented radiator, the spatial frequencies entering the form factor must account for the geometry of the electron–radiator interaction. For a radiator tilted by 45° with respect to the electron beam, the form factor may be written as

$$|f|^2 = \exp\left(-\sigma_x^2 \Delta k_x^2\right) \exp\left(-\sigma_y^2 {k'_y}^2\right) \exp\left(-\sigma_z^2 {k'_z}^2\right), \tag{3.16}$$

where the effective wave-vector components are given in Eqs. 3.8, 3.9, and 3.10.

Unlike the normal-incidence case, the transverse contribution cannot in general be represented by a single quantity, since the tilted geometry breaks the symmetry between the two transverse directions. In the plane of incidence, $\phi = 0°$, the x-dependent suppression is minimized when $\Delta k_x \approx 0$, corresponding to

$$\sin\theta \approx \frac{1}{\sqrt{2}\beta}. \tag{3.17}$$

For highly relativistic electrons, for which $\beta \approx 1$, this condition occurs near $\theta = 45°$. Thus, the Gaussian form factor remains smoothly and monotonically decreasing with increasing phase mismatch, but its angular dependence is determined by the wave-vector components associated with the tilted radiator rather than by the normal-incidence longitudinal and transverse wave vectors.

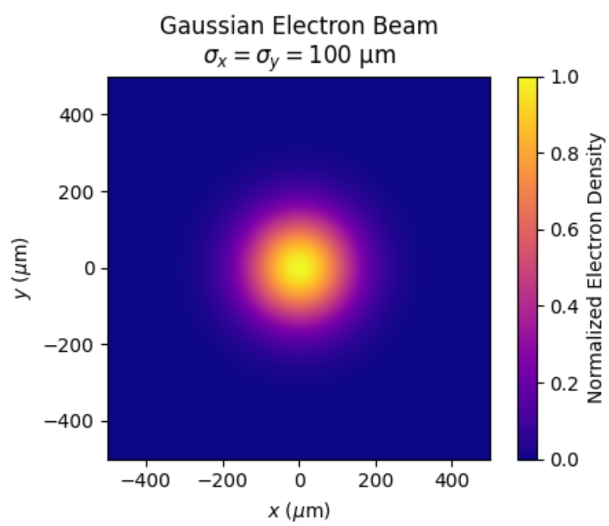

Figure 3.1: Normalized transverse electron density of a Gaussian bunch with $\sigma_x = \sigma_y = 100\,\mu$m. The horizontal and vertical axes are the transverse coordinates x and y in micrometers. Color represents the transverse density normalized to its peak value, $\rho_T/\max(\rho_T)$, so the displayed range is 0–1.

3.4.2 Longitudinally Incoherent and Coherent Regimes

At $\tau = 1$ ns, the longitudinal bunch size, $\sigma_L = c\tau$, is many orders of magnitude larger than the wavelengths considered in the simulated NIR–MIR band. The longitudinal phase variation across the bunch is characterized by

$$k_z\sigma_z = \frac{2\pi c\tau}{\lambda}, \tag{3.18}$$

which is much greater than unity throughout the simulated wavelength range. Consequently, the longitudinal form factor is exponentially suppressed and the coherent contribution to the bunch radiation becomes negligible. The bunch spectrum therefore approaches

$$W_n \approx N_e W_1, \tag{3.19}$$

where W_1 is the single-electron transition-radiation spectrum for the 45° tilted interface. Thus, in this limit, the observed angular distribution retains the angular structure imposed by the tilted radiator geometry and is scaled linearly by the number of electrons in the bunch.

At $\tau = 1\,\mathrm{fs}$, the longitudinal bunch size is approximately $\sigma_L \approx 0.3\,\mu\mathrm{m}$ for a relativistic electron beam. The bunch is therefore substantially more coherent over the simulated spectral range; however, it is not fully coherent at all wavelengths. For a Gaussian longitudinal distribution, the coherence scale is obtained from $k_z\sigma_z = 1$, giving

$$\lambda_c = 2\pi c\tau. \tag{3.20}$$

For $\tau = 1\,\mathrm{fs}$, this corresponds to $\lambda_c \approx 1.88\,\mu\mathrm{m}$. At wavelengths significantly larger than this value, the longitudinal form factor approaches unity, whereas at shorter wavelengths the finite bunch duration produces noticeable suppression.

In the limit that $|f|^2 \to 1$, the bunch radiation approaches

$$W_n = W_1\left[N_e + N_e(N_e-1)|f|^2\right] \approx N_e^2 W_1. \tag{3.21}$$

For a bunch charge of $5\,\mathrm{pC}$, $N_e \approx 3.1 \times 10^7$. The fully coherent contribution therefore scales quadratically with electron number and is approximately N_e times larger than the corresponding incoherent bunch contribution. This quadratic scaling is the characteristic superradiant enhancement of coherent transition radiation.

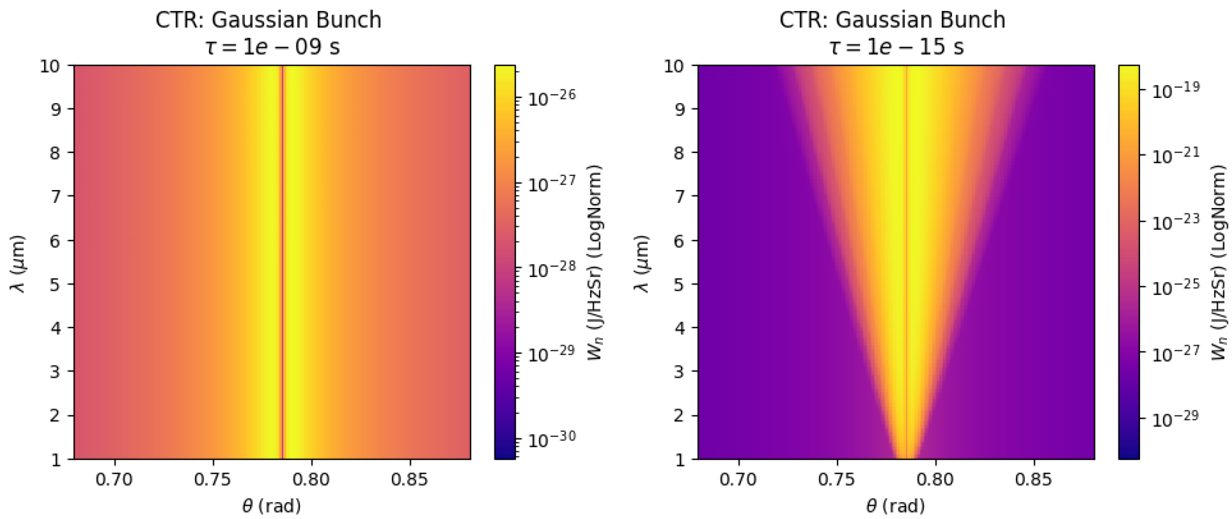

Figure 3.2: Spectral-angular CTR distribution W_n for a Gaussian electron bunch with $\tau = 1\,\mathrm{ns}$ (left) and $\tau = 1\,\mathrm{fs}$ (right). The horizontal axis is the observation angle θ in radians, and the vertical axis is wavelength λ in micrometers, sampled linearly from 1 to 10 μm. The plotted quantity is W_n evaluated at $\omega = \frac{2\pi c}{\lambda}$ and reported in $J/(Hz \cdot Sr)$; color is displayed using logarithmic normalization (LogNorm), not peak normalization of W_n. The two panels use independent color limits.

3.4.3 Coherence Roll-Off ($\tau = 5\,\mathrm{fs}$)

At $\tau = 5\,\mathrm{fs}$, we are within the diagnostic regime. The coherence edge sits at $\lambda_c \sim 2\pi\sigma_L$, which corresponds to the wavelength at which $k_L\sigma_L = 1$. For $\tau = 5\,\mathrm{fs}$, this corresponds to $\lambda_c \sim 9\,\mu\mathrm{m}$, which is inside the simulated NIR-MIR band. The visible roll-off is primarily governed by the phase-matched angular direction introduced by the tilted radiator. Namely, at $\phi = 0°$, $\Delta k_x = \frac{2\pi}{\lambda}(\sqrt{2}\sin\theta - \frac{1}{\beta})$. For a relativistic beam, $\beta \sim 1$, so Δk_x is approximately zero when $\sqrt{2}\sin\theta = 1$ or $\theta \sim 45° = 0.79\,\mathrm{rad}$. It is exactly at this angle that radiation is least suppressed. Radiation will be progressively suppressed as the observation angle deviates from the phase-matched angle.

For a Gaussian bunch, the three-dimensional form factor remains the product of independent Gaussian factors. However, the observable spectral and angular dependencies are not completely independent. This is due to the transverse phase mismatch, which depends on both wavelength and observation angle. Near the phase-matched direction, where the transverse mismatch is small, the wavelength dependence is primarily governed by the longitudinal bunch duration and can therefore provide sensitivity to σ_L. Away from this direction, the measured spectrum contains contributions from both the longitudinal and the transverse form factors.

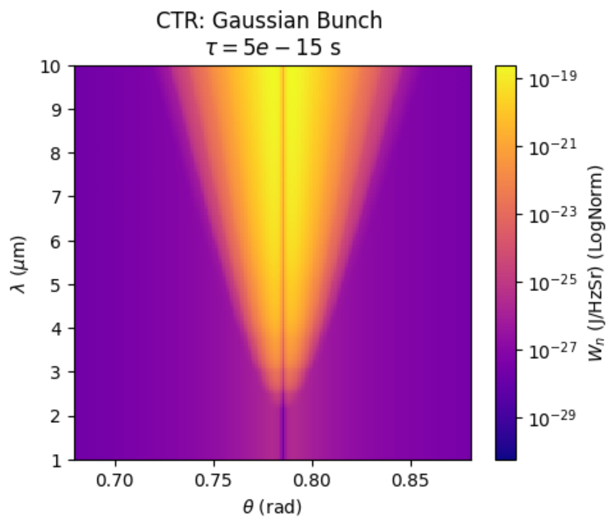

Figure 3.3: Spectral-angular CTR distribution W_n for a Gaussian electron bunch with $\tau = 5\,\mathrm{fs}$. The horizontal axis is the observation angle θ in radians, and the vertical axis is wavelength λ in micrometers, linearly sampled from 1 to 10 μm. W_n is evaluated at $\omega = \frac{2\pi c}{\lambda}$ and displayed in $J/(Hz \cdot Sr)$ using logarithmic color normalization; the radiation values are not peak normalized. The wavelength-dependent narrowing illustrates the coherence roll-off and the preferential emission near the phase-matched direction $\theta \approx 0.79\,\mathrm{rad}$.

3.5 Three-Dimensional Hollow Gaussian Electron Beams

We next consider a family of hollow Gaussian electron bunches. Recall that p is a nonnegative integer controlling the radial structure of the bunch. For $p = 0$, the distribution reduces to the conventional three-dimensional Gaussian. For $p > 0$, the factor $(x^2 + y^2)^p$ suppresses the charge density near the beam axis and produces an annular transverse profile. Increasing p therefore increases the radius of the hollow region while preserving azimuthal symmetry.

It is important to distinguish this distribution from that of an orbital angular momentum electron beam. The hollow Gaussian density considered here is a real, nonnegative charge distribution and contains no azimuthally varying phase factor. Consequently, p does not represent topological charge, and the bunch does not possess a phase singularity or orbital angular momentum as a consequence of this density profile alone.

For the cylindrically symmetric case, $\sigma_x = \sigma_y = \sigma_T$, the transverse distribution may be written in terms of $r^2 = x^2 + y^2$ as

$$\rho_T \propto r^{2p} \exp\left(-\frac{r^2}{2\sigma_T^2}\right). \tag{3.22}$$

The maximum of the transverse charge density occurs at

$$r_{\max} = \sigma_T \sqrt{2p}, \tag{3.23}$$

for $p > 0$, illustrating that increasing p progressively shifts the electron density away from the bunch axis. The normalized transverse Fourier transform of this distribution is

$$f_T(q_T) = \exp\left(-\frac{\sigma_T^2 q_T^2}{2}\right) L_p\left(\frac{\sigma_T^2 q_T^2}{2}\right), \tag{3.24}$$

where L_p is the Laguerre polynomial of order p and q_T is the effective transverse spatial frequency sampled by the radiation. The corresponding three-dimensional form factor is therefore

$$|f|^2 = \exp\left(-\sigma_T^2 q_T^2\right) \left[L_p\left(\frac{\sigma_T^2 q_T^2}{2}\right)\right]^2 \exp\left(-\sigma_z^2 k_z'^2\right). \tag{3.25}$$

For the 45° tilted radiator considered throughout this work, the transverse spatial frequency is evaluated using the transformed Fourier coordinates introduced in Section 3.2,

$$q_T^2 = \Delta k_x^2 + k_y'^2, \tag{3.26}$$

where

$$\Delta k_x = \sqrt{2}\frac{\omega}{c}\sin\theta\cos\phi - \frac{\omega}{v}, \tag{3.27}$$

$$k'_y = \frac{\omega}{c}\sin\theta\sin\phi, \qquad k'_z = \frac{\omega}{v}. \tag{3.28}$$

Thus, the hollow Gaussian transverse structure modifies the CTR spectrum through the Laguerre-polynomial dependence of the bunch form factor, while the location of the phase-matched radiation direction continues to be determined by the tilted-interface geometry.

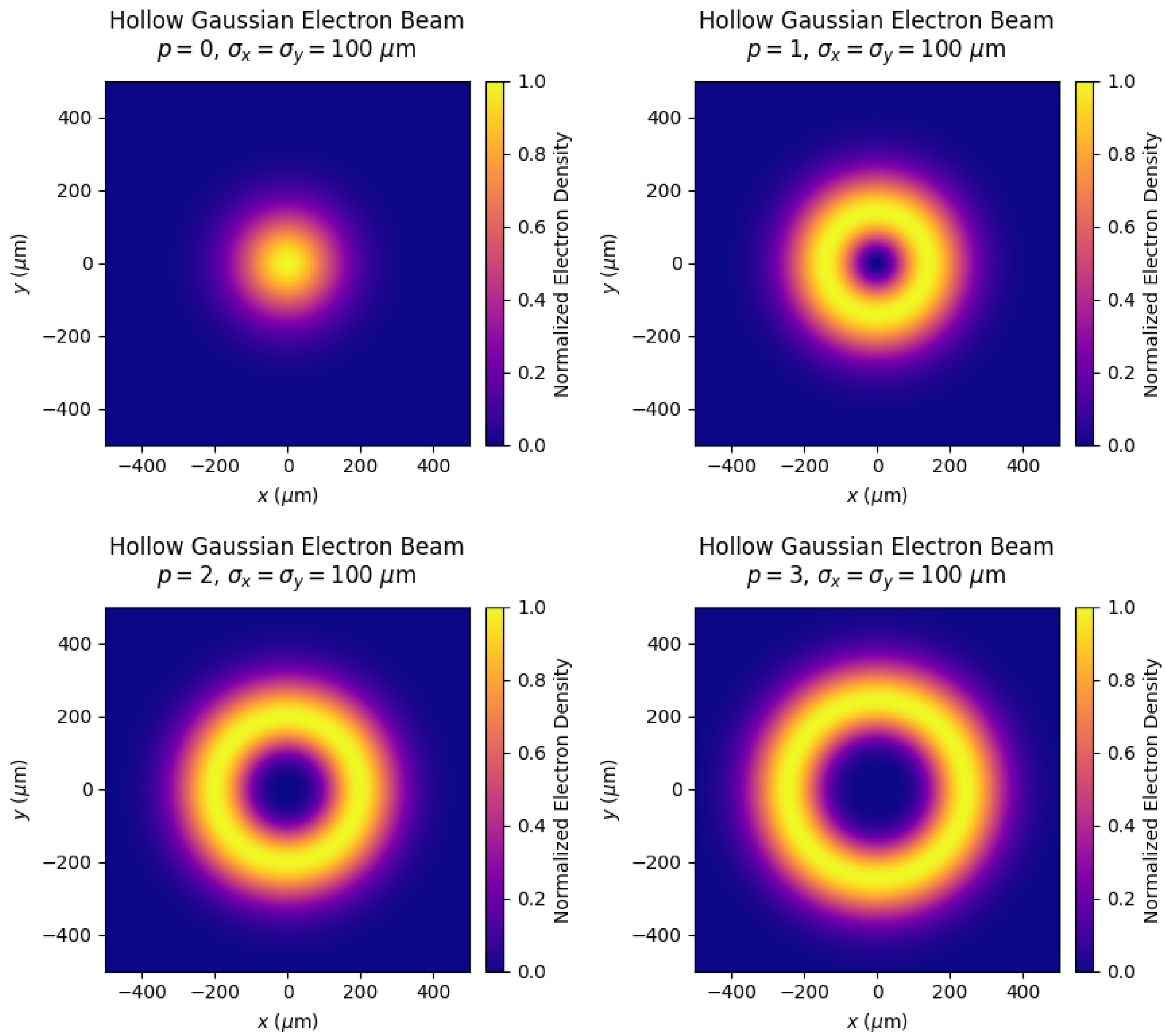

Figure 3.4: Normalized transverse electron-density distributions for hollow Gaussian bunches with radial-order parameters $p = 0$, 1, 2, and 3 and $\sigma_x = \sigma_y = 100\,\mu$m. The horizontal and vertical axes are x and y in micrometers. Each distribution is independently peak-normalized to unity, while all panels use the common displayed color range of 0–1. Consequently, the colors compare spatial shapes rather than absolute electron densities across orders. Increasing p moves the maximum density outward and produces an increasingly large annular region.

3.5.1 Radial-Order Dependence of the Angular Pattern

Unlike an electron bunch carrying orbital angular momentum, the hollow Gaussian distribution does not force the form factor to vanish at zero transverse spatial frequency. In fact,

$$f_T(0) = L_p(0) = 1 \tag{3.29}$$

for every value of p. Therefore, although the real-space electron density contains an increasingly pronounced central hollow for $p > 0$, the corresponding CTR form factor is not required to contain a central null. This distinction follows from the fact that the zero-spatial-frequency component of the normalized Fourier transform represents the total charge of the bunch and is therefore unity. Instead, the characteristic angular structure of the hollow Gaussian bunch arises from the zeros and oscillations of the Laguerre polynomial in the transverse form factor. For $p = 0$, $L_0 = 1$ and the distribution reduces to the conventional Gaussian result. For $p > 0$, the polynomial introduces zeros at finite values of q_T, producing regions in which the coherent contribution to the CTR spectrum is suppressed. As p increases, additional zeros appear and the angular spectrum develops an increasing number of bright and dark features.

For the 45° tilted interface and the $\phi = 0$ observation plane used here,

$$q_T = \left| \frac{2\pi}{\lambda} \left(\sqrt{2} \sin\theta - \frac{1}{\beta} \right) \right|. \tag{3.30}$$

For a highly relativistic electron beam, for which $\beta \approx 1$, this quantity approaches zero near $\theta = 45°$. Consequently, all values of p retain a strong coherent contribution near the phase-matched direction. Away from this angle, q_T increases and the Laguerre-polynomial structure of the hollow Gaussian form factor becomes increasingly apparent. The multiple angular bands observed for larger p therefore originate from the radial structure of the real charge distribution and its Fourier transform, rather than from a phase singularity or topological charge.

Because q_T is proportional to $1/\lambda$, the positions of these form-factor minima are also wavelength dependent. The resulting features therefore appear as angled or diverging bands in the (θ, λ) CTR spectrum. Increasing p adds additional transverse spatial scales to the bunch and consequently produces additional form-factor minima and maxima in the radiation pattern.

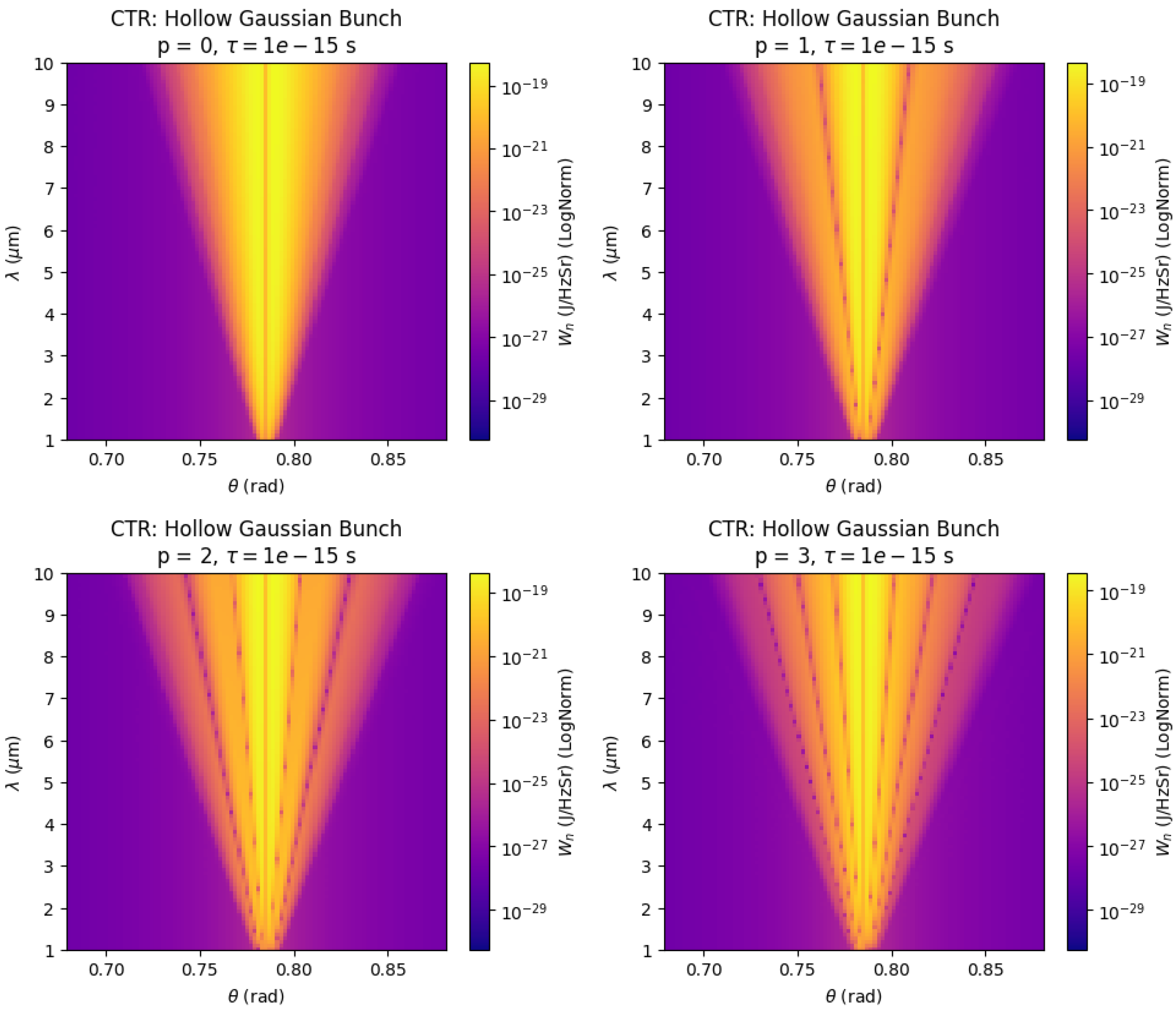

Figure 3.5: Spectral-angular CTR distributions W_n from hollow Gaussian electron bunches with $p = 0$, 1, 2, and 3 and $\tau = 1\,\text{fs}$. The horizontal axis is the observation angle θ in radians, and the vertical axis is wavelength λ in micrometers, linearly sampled from 1 to 10 μm. W_n is evaluated at $\omega = \frac{2\pi c}{\lambda}$ and reported in $(J/Hz \cdot Sr)$, with logarithmic color normalization and no peak normalization of the radiation intensity. All four panels use common color limits, allowing direct comparison of absolute radiation levels. Increasing p introduces additional wavelength-dependent bright and dark angular bands associated with the zeros and oscillations of the hollow-Gaussian form factor. At the same time, strong emission remains near the phase-matched direction around $\theta \approx 0.79\,\text{rad}$.

3.6 Three-Dimensional Airy Electron Beams

The finite-energy Airy bunch is modeled at the radiator using a real, nonnegative charge density of the form

$$\rho(x, y, z) = \rho(x, y; z_{\text{prop}}), \tag{3.31}$$

where $\rho = |\psi_{\text{Airy}}|^2$ describes the propagated transverse Airy distribution. The Airy propagation coordinate z_{prop} therefore specifies the distance over which the transverse distribution evolves before reaching the radiator and is distinct from the usual longitudinal bunch coordinate z, which determines arrival-time coherence. The transverse form factor may be expressed as

$$|f| = f_T(\Delta k_z, k'_y). \tag{3.32}$$

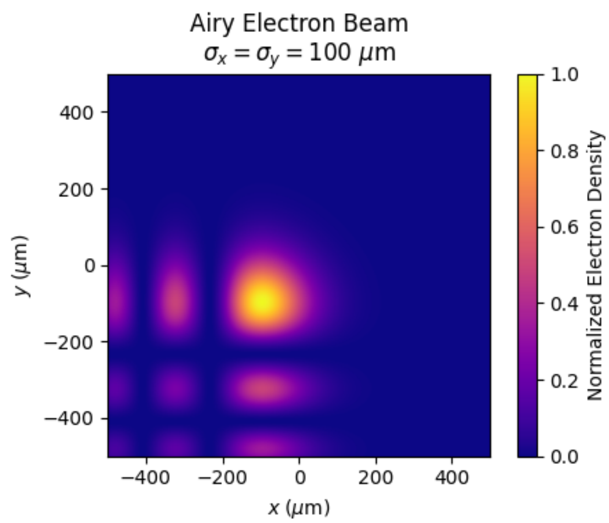

Figure 3.6: Normalized transverse electron density of the finite-energy Airy bunch at the radiator for $\sigma_x = \sigma_y = 100\,\mu$m. The horizontal and vertical axes are x and y in micrometers. The plotted quantity is the real, nonnegative transverse density $\rho_T = |\psi_{Airy}|^2$, normalized to its maximum value; the color scale therefore spans 0–1.

3.6.1 Spectral Response of Airy Bunches with Varying Propagation Lengths and Apodization

The weak dependence of the CTR intensity pattern on Airy propagation distance follows from the characteristic Airy propagation scale.

$$L_A = k_e \sigma_x^2, \qquad \xi = \frac{z_{\text{prop}}}{L_A}. \tag{3.33}$$

For a finite-energy Airy distribution, the dominant propagation effect at small $\alpha\xi$ is the parabolic transverse displacement.

$$\Delta x = \frac{z_{\text{prop}}^2}{4k_e^2 \sigma_x^3} = \frac{\sigma_x \xi^2}{4}. \tag{3.34}$$

However, a translation of the charge density does not modify the magnitude of its Fourier transform. Specifically,

$$\rho(x - \Delta x) \xrightarrow{\mathcal{F}} e^{-i\Delta k_x \Delta x} \widetilde{\rho}(\Delta k_x), \tag{3.35}$$

and therefore

$$\left| e^{-i\Delta k_x \Delta x} \widetilde{\rho}(q_x) \right|^2 = |\widetilde{\rho}(\Delta k_x)|^2. \tag{3.36}$$

Thus, although the Airy bunch may move substantially in real space, this trajectory alone cannot alter the CTR intensity form factor. After this translation is removed, the normalized finite-energy Airy density depends primarily on the dimensionless quantity:

$$a\xi = a \frac{z_{\text{prop}}}{k_e \sigma_x^2}. \tag{3.37}$$

For a 100 MeV electron beam with $\sigma_x = 100\,\mu$m, the electron wavenumber gives

$$k_e \sigma_x^2 \simeq 5.09 \times 10^{10} \text{ m}. \tag{3.38}$$

At $z_{\text{prop}} = 10^6$ m,

$$\xi \simeq 2, \qquad \alpha\xi \simeq 0.1 \tag{3.39}$$

for $\alpha = 0.05$. The Airy distribution is therefore predominantly translated rather than significantly deformed, unless propagated over extreme propagation distances, as seen in Fig. 3.7.

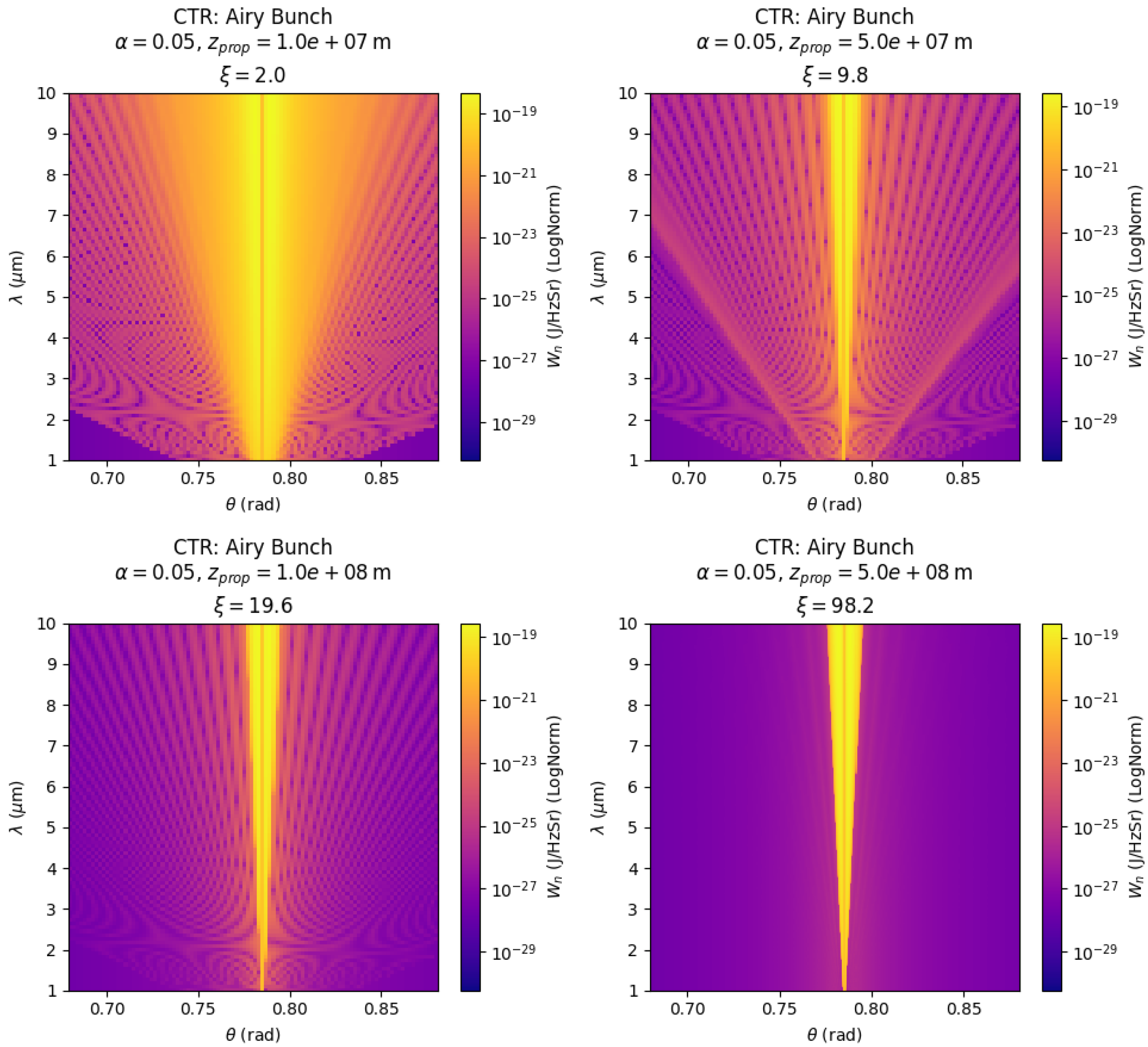

Figure 3.7: Spectral-angular CTR distributions W_n for an Airy electron bunch with apodization $\alpha = 0.05$ at propagation distances $z_{prop} = 1 \times 10^7, 5 \times 10^7, 1 \times 10^8$ and 5×10^8 m corresponding to normalized propagation coordinates $\xi = 2.0, 9.8, 19.6,$ and 98.2, respectively. The horizontal axis is the observation angle θ in radians, and the vertical axis is wavelength λ in micrometers, linearly sampled from 1 to 10 μm. W_n is evaluated at $\omega = \frac{2\pi c}{\lambda}$ and displayed in $J/(Hz \cdot Sr)$ with logarithmic color normalization. The panels use common color limits and are not individually peak-normalized, permitting direct intensity comparison. Increasing propagation distance substantially changes the fine spectral-angular fringe structure while retaining strong emission near the phase-matched angular direction.

This provides a useful pedagogical contrast with the Gaussian case, whose spectral envelope is set directly by the longitudinal bunch size σ_L. As the apodization level α increases, the

Airy CTR spectrum becomes increasingly Gaussian-like.

The propagation insensitivity of $|f|^2$ also has a sharp consequence: an Airy bunch's propagation coordinate z_{prop} is not recoverable from an intensity-only CTR measurement after a certain propagation distance. Recovering it would require a phase-sensitive measurement (e.g., interferometric CTR or coherent detection against a reference). Conversely, from a source-design perspective, the propagation insensitivity is an asset: an Airy-shaped bunch produces a CTR spectrum that is robust against drift in the longitudinal observation position, a property no Gaussian bunch shares.

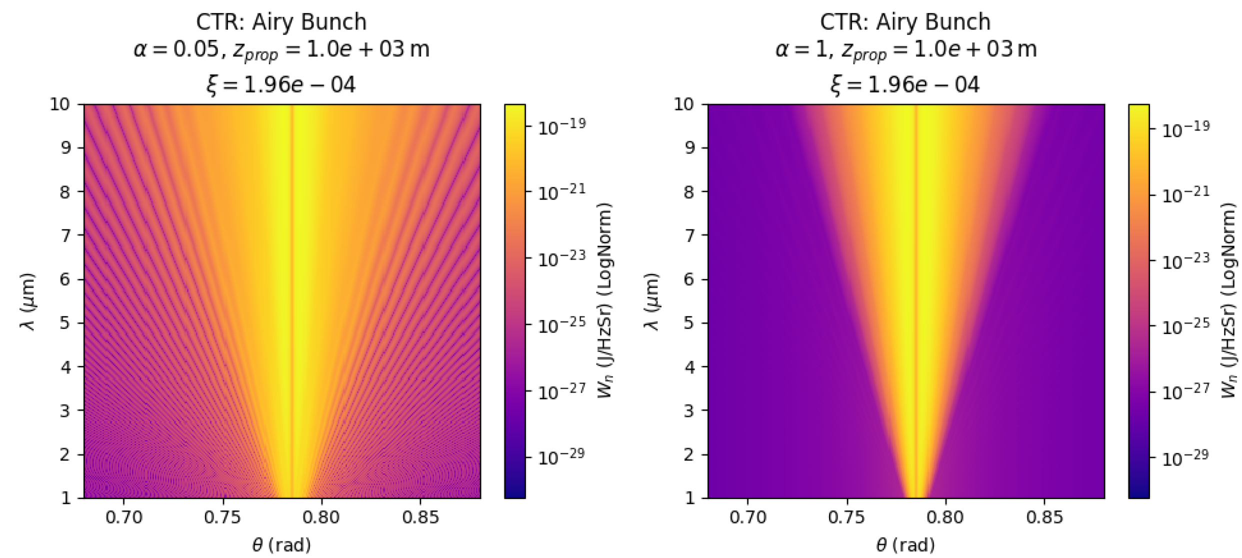

Figure 3.8: Spectral-angular CTR distributions W_n for Airy electron bunches with apodization parameters $\alpha = 0.05$ (left) and $\alpha = 1$ (right), evaluated at $z_{prop} = 1\times10^3$ m and $\xi = 1.96\times10^{-4}$. The horizontal axis is the observation angle θ in radians, and the vertical axis is wavelength λ in micrometers, linearly sampled from 1 to 10 μm. W_n is evaluated at $\omega = \frac{2\pi c}{\lambda}$ and reported in $J/(Hz \cdot Sr)$ using logarithmic color normalization. The two panels use the same color limits and are not independently peak-normalized. Weak apodization retains pronounced Airy interference structure, whereas stronger apodization suppresses the secondary structure and produces a smoother, Gaussian-like spectral-angular envelope.

3.7 Longitudinal Coherence

While the CTR spectrum provides a direct view of the emitted radiation, the coherence properties of the electron bunch fundamentally govern its spectral structure. In particular, the onset and extent of coherent emission are strongly determined by the longitudinal bunch profile, motivating a closer examination of longitudinal coherence.

Consider an arbitrary spatial electron distribution with distinct transverse and longitudinal profiles, as developed in Section 2.2.1. Recall that the form factor of this distribution is given by

$$f^2 = f_T^2 f_L^2. \tag{3.40}$$

Moreover, f_T is given by

$$f_T = \int \int \rho_T(x, y) e^{i(k_x x + k_y y)} dx dy. \tag{3.41}$$

Notably, the phase of f_T is given by $\phi_T = k_x x + k_y y$. If the spatial distribution has transverse size σ_T, then the electrons within the bunch acquire a phase difference of $\Delta\phi_T \sim k_T \sigma_T$, where $k_T = \sqrt{k_x^2 + k_y^2} = \frac{2\pi}{\lambda_c} \sin\theta$. For the radiation from each electron to add coherently, their respective phases should not vary by more than approximately one radian. We therefore impose

$$k_T \sigma_T \lesssim 1 \tag{3.42}$$

Using these expressions, we obtain

$$\frac{2\pi\sigma_T \sin\theta}{\lambda_c} \lesssim 1. \tag{3.43}$$

For small observation angles, using the fact that radiation is concentrated around angles given by $\theta \sim \frac{1}{\gamma}$, we obtain

$$\frac{2\pi\sigma_T}{\gamma} \lesssim \lambda_c. \tag{3.44}$$

That is, if the aforementioned quantity is less than the coherence threshold wavelength, λ_c, transverse coherence is negligible. Moreover, using the values in Table 3.1, we find that the left-hand side of Eq. 3.44 is indeed much smaller than the coherent radiation wavelengths of interest. We may therefore focus on longitudinal coherence as transverse coherence is suppressed.

Moreover, consider the longitudinal profiles of each of the spatial distributions highlighted in Section 3.3:

$$\rho_L(z) = \exp\left(-\frac{z^2}{2\sigma_z^2}\right). \tag{3.45}$$

To consider longitudinal coherence, the CTR spectrum, W_n, as given in (2), must be separated into its coherent and incoherent contributions. Namely,

$$W_n = W_{incoherent} + W_{coherent} \tag{3.46}$$

$$W_{incoherent} = N_e W_1 \tag{3.47}$$

$$W_{coherent} = N_e(N_e - 1)|f^2|W_1. \tag{3.48}$$

The ratio is therefore

$$\frac{W_{coherent}}{W_{incoherent}} = (N_e - 1)|f^2|. \tag{3.49}$$

The onset of coherence according to this criterion occurs when $W_{coherent} = W_{incoherent}$. The following plots were generated based on the preceding analysis.

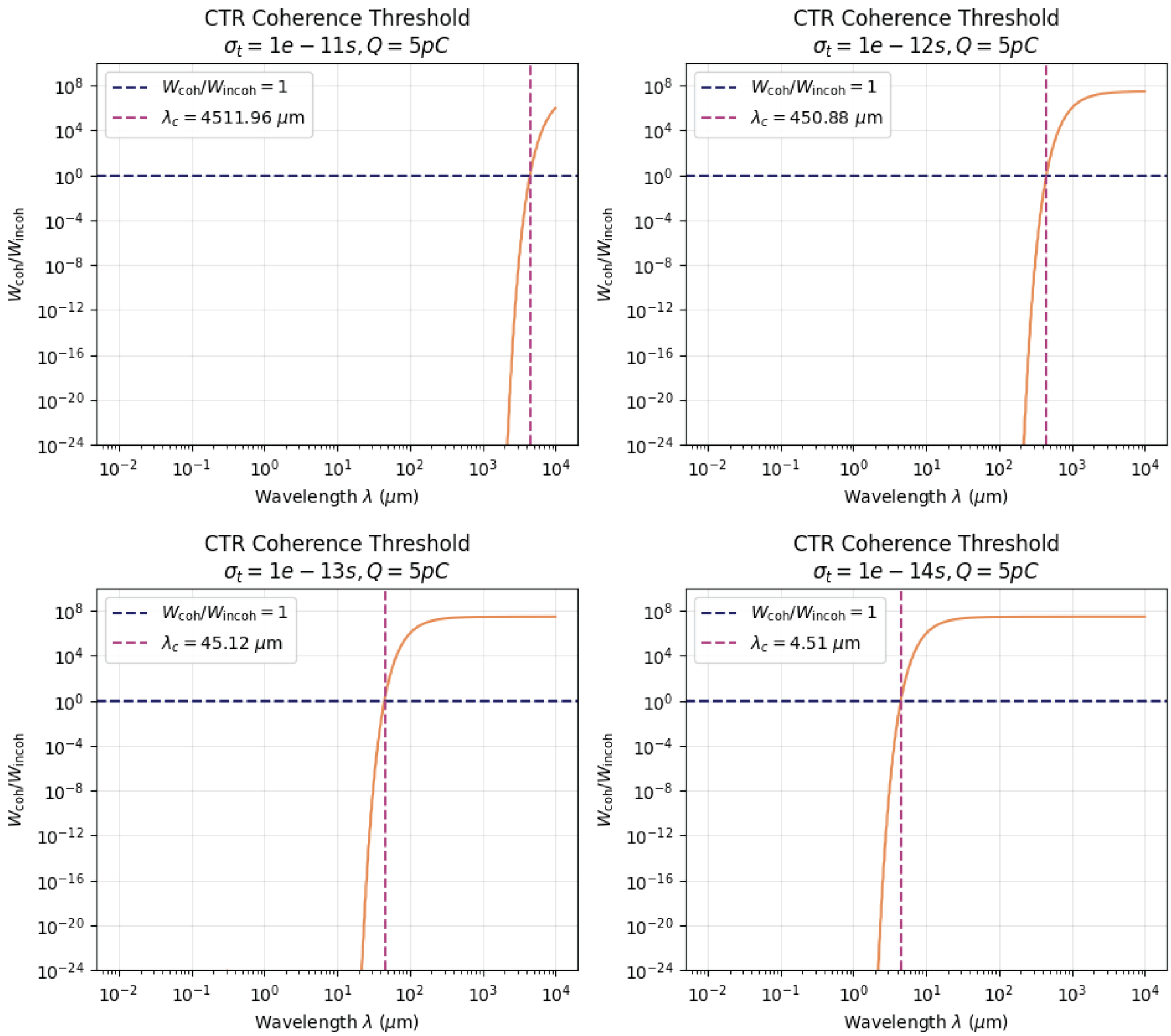

Figure 3.9: Longitudinal coherence threshold for Gaussian electron bunches with $Q = 5\,\text{pC}$ and RMS temporal durations $\sigma_t = 10\,\text{ps}, 1\,\text{ps}, 100\,\text{fs}$, and $10\,\text{fs}$. Each panel plots the dimensionless coherent-to-incoherent radiation ratio $\frac{W_{coh}}{W_{icoh}} = (N_e - 1)|f|^2$ versus wavelength λ in micrometers. Both axes are logarithmic. The horizontal dashed line marks $\frac{W_{coh}}{W_{incoh}} = 1$, which defines the onset of coherence, and the vertical dashed lines indicate the corresponding threshold wavelengths $\lambda_c = 4511.96, 450.88, 45.12,$ and $4.51\,\mu\text{m}$.

3.8 A Unifying Observation

Read together, the three case studies illustrate that the form factor acts as the master variable governing not just the amount of coherent radiation but its spectral, angular, and informational structure. The Gaussian provides a smooth coherence envelope; the hollow Gaussian bunch reshapes the angular distribution while conserving integrated intensity; the Airy bunch sacrifices a tunable amplitude envelope in exchange for propagation-invariant intensity. The same numerical pipeline, applied to any user-supplied 3D distribution, will produce analogous interpretations, with each spectrum's features traceable to the analytical structure of $|f(\bar{k})|^2$ for the corresponding source.

Chapter 4

Experimental Application: Coherent Transition Radiation from Single-Digit-Femtosecond Electron Beam Structure

4.1 Experimental Motivation and Overview

The computational framework developed in Chapter 3 provides a means of mapping an assumed electron-bunch distribution to its corresponding coherent transition radiation spectrum. In addition to predicting the radiation produced by arbitrary electron-bunch structures, this framework can be used in reverse: experimentally measured radiation spectra can be compared with simulated spectra to constrain the properties of the electron bunch responsible for the emission. As such, an experimental campaign conducted at Deutsches Elektronen-Synchrotron (DESY) during the summer of 2025 provided an opportunity to further investigate CTR under strongly compressed beam conditions by applying the numerical framework developed in Chapter 3 to experimentally measured radiation spectra. The results of this collaborative experiment were subsequently reported in [1]. The experiment observed coherent emission extending into the visible spectrum and used the CTR model developed in this work to infer the characteristic longitudinal structure of the emitting electron bunch.

The experiment demonstrated optical-frequency coherent transition radiation following strong longitudinal compression in a conventional radio-frequency linear accelerator. Unlike many previous observations of visible CTR associated with free-electron-laser interactions or optically induced microbunching, the observed radiation was generated without an undulator, FEL interaction, or externally imposed optical modulation. The measured optical spectra exhibited a nonlinear dependence on bunch charge, with an approximately quadratic contribution over a substantial portion of the visible spectrum, providing experimental evidence of superradiant emission from ultrashort longitudinal electron-beam structure.

The importance of this experiment within the context of the present thesis is twofold. First, it provides an experimental demonstration of the longitudinal-coherence behavior discussed in Section 3.7. Second, and more importantly, the numerical CTR framework developed in Chapter 3 was used to construct the spectral models used to fit the measured data. Whereas Chapter 3 considered the forward problem—beginning with an electron-bunch distribution and calculating the emitted CTR spectrum—the experimental analysis presented here applies the same relationship in reverse. A family of simulated spectra was generated for different longitudinal bunch durations and compared with the measured optical spectra, allowing a characteristic longitudinal timescale of the electron bunch to be inferred.

4.2 Experimental Production of CTR at ARES

The experimental measurements were performed at the Accelerator Research Experiment at SINBAD (ARES) facility at DESY. ARES employs an S-band photoinjector followed by traveling-wave accelerating structures and a magnetic bunch compressor to produce ultrashort relativistic electron bunches. For the measurements considered here, the electrons had a kinetic energy of approximately 120 MeV. An X-band transverse deflecting structure located near the CTR target provided an independent measurement of the bunch duration; this measurement was resolution-limited to approximately 4 fs RMS.

Transition radiation was generated using a silver mirror positioned at an incidence angle of 45° with respect to the electron trajectory. In this geometry, backward transition radiation was directed approximately 90° away from the electron-beam propagation direction, permitting the optical radiation to be extracted through a viewport. At the same time, the electron beam continued through the beamline. The spatial radiation distribution was recorded using a CMOS camera, while wavelength-resolved measurements were obtained using a fiber-coupled spectrometer covering approximately 200–1100 nm.

Longitudinal compression of the electron bunch was achieved by using the second traveling-wave structure (TWS2) to impose a controlled energy chirp on the beam before it was transported through the magnetic bunch compressor. By varying the phase of TWS2 relative to the maximum momentum-gain phase, the longitudinal phase space—and therefore the degree of compression—could be adjusted. For the CTR spectral analysis, measurements were taken at TWS2 phases of 32°, 33°, and 34°. These three operating points produced different measured radiation intensities while yielding very similar fitted longitudinal bunch durations of approximately 1.2 fs, thereby enabling evaluation of the consistency of the CTR-based bunch-length inference across neighboring compression settings. For each operating condition, spectra were averaged over 100 consecutive electron bunches, and a background spectrum obtained with the electron beam blocked was subtracted from the measurements.

4.3 Application of Computational Framework to Experimental Observables

To further highlight the pipeline developed to predict longitudinal coherence, we next compare the predicted onset with previously reported results. In [1], Pennington et al. reported the first observation of CTR from ultrashort, relativistic electron bunches. The superradiant optical transition radiation was measured over the 550-800 nm spectral range. The captured radiation exhibited quadratic scaling, confirming that the emission was indeed coherent and governed by the longitudinal bunch form factor.

The Gaussian spectral envelope developed throughout the computational framework was used directly as the predicted radiation response for comparison with the experimentally measured CTR spectra. Rather than fitting the experimental data with an arbitrary empirical function, the model begins with an assumed Gaussian longitudinal electron-bunch distribution and calculates its corresponding form factor and coherent transition-radiation spectrum. The longitudinal bunch duration therefore controls the spectral roll-off: shorter bunches retain a large form factor to higher frequencies, extending coherent emission toward shorter wavelengths, whereas longer bunches lose coherence earlier. By varying the assumed bunch duration, a family of predicted Gaussian CTR spectra was generated and compared with the measured spectral envelopes. This procedure produced characteristic longitudinal structures of approximately 1.22–1.26 fs in the measured spectra across different compression phases, demonstrating that the experimentally observed spectral shape is consistent with a single-digit-femtosecond electron-beam structure.

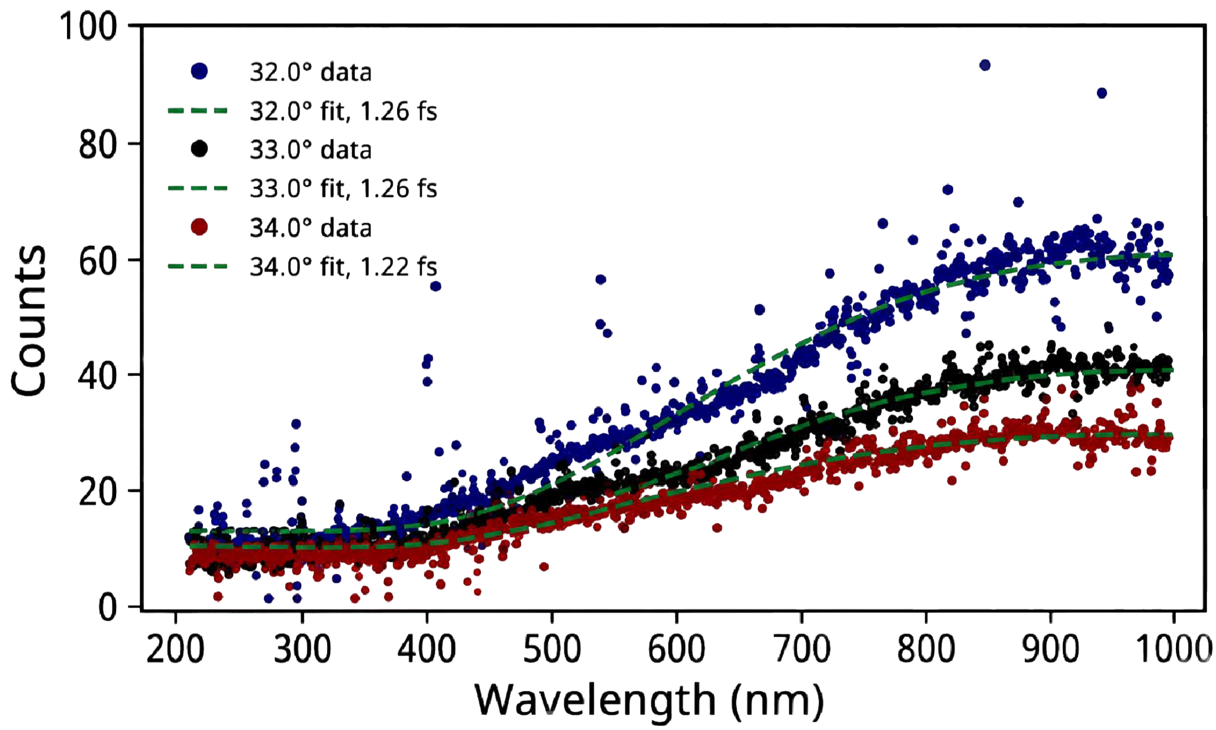

Figure 4.1: Measured wavelength-resolved CTR spectra and Gaussian-model fits for TWS2 phases of 32°, 33°, and 34°. The horizontal axis is wavelength in nanometers on a linear scale, spanning approximately 200–1000 nm, and the vertical axis is detector counts on a linear scale. Colored points show the measured, background-subtracted spectra, and dashed green curves show Gaussian CTR-model fits corresponding to RMS bunch durations of 1.26 fs, 1.26 fs, and 1.22 fs for 32°, 33°, and 34°, respectively. The measured spectra were averaged over 100 consecutive electron bunches. The detector counts are not normalized, and no color scale or color limits apply [1].

The same Gaussian model can also be used to identify the wavelength at which the coherent contribution becomes comparable to the incoherent transition-radiation background. In the simulation shown in Fig. 4.2, the coherent-to-incoherent intensity ratio, $W_{\mathrm{coh}}/W_{\mathrm{incoh}}$, is evaluated for a characteristic bunch duration of approximately 1.2 fs. Defining the onset of coherence by $W_{\mathrm{coh}}/W_{\mathrm{incoh}} = 1$, the model predicts a coherence threshold of approximately $\lambda_c = 0.55\,\mu\mathrm{m}$, or 550 nm. This predicted transition is particularly significant because the experimental charge-scaling analysis independently identifies the onset of a coherence-dominated regime at approximately 550 nm, above which the measured intensity is well described by the quadratic charge dependence expected for coherent emission. Thus, the agreement between the simulated Gaussian coherence threshold and the experimentally observed onset of superradiant scaling provides an additional validation of the numerical CTR framework.

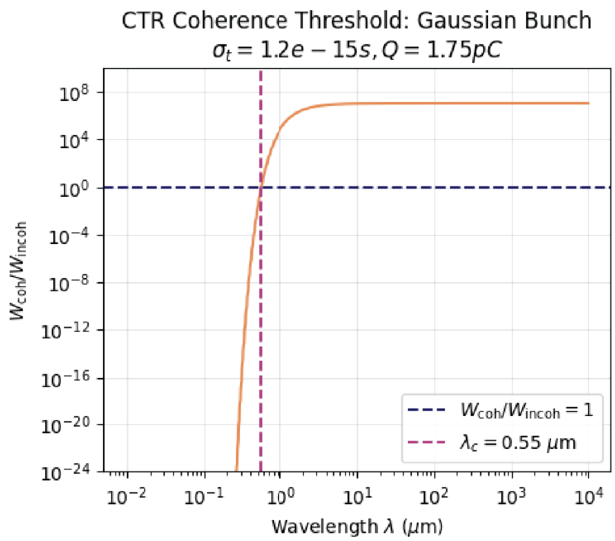

Figure 4.2: Predicted longitudinal coherence threshold for a Gaussian electron bunch with $\sigma_t = 1.2\,\text{fs}$ and $Q = 1.75\,\text{pC}$. The horizontal axis is wavelength λ in micrometers on a logarithmic scale, and the vertical axis is the dimensionless coherent-to-incoherent CTR ratio $\frac{W_{coh}}{W_{incoh}}$ on a logarithmic scale. The horizontal dashed line denotes $\frac{W_{coh}}{W_{incoh}} = 1$, and the vertical dashed line marks the predicted coherence threshold $\lambda_c = 0.55\,\mu\text{m}$. The ratio is not additionally normalized, and no color scale is used. The predicted threshold coincides with the experimentally observed onset of coherence-dominated charge scaling near 550 nm.

Chapter 5

Conclusion

We have presented a tutorial-style, simulation-first treatment of coherent transition radiation that takes the bunch form factor $|f(k)|^2$ as the central organizing object. Starting from the Ginzburg–Frank single-electron formula, we derived the coherent enhancement that arises for an N_e-electron bunch, made the geometric corrections required for realistic experiments (finite radiator, 45° tilt, formation length) explicit, and implemented the result as an open numerical pipeline that maps any user-supplied three-dimensional charge distribution onto an angle- and wavelength-resolved CTR spectrum. The three case studies — Gaussian, hollow Gaussian, and Airy — were chosen not for their novelty as bunch geometries but for what they reveal about the form factor's role as the master variable governing coherent emission.

Together, the three cases make a single mechanistic point. The Gaussian bunch sets a smooth coherence envelope in which longitudinal and transverse contributions to $|f(k)|^2$ act independently, producing the textbook bunch-length and angular-divergence diagnostics. The hollow Gaussian bunch reshapes the distribution into lobes with nulls directly traceable to the structure of the form factor — meaning the form factor redistributes coherent radiation in k-space rather than amplifying or attenuating it. The Airy bunch, by contrast, is modeled over the propagation range for which the Airy profile is predominantly translated rather than substantially deformed; changes in propagation distance primarily introduce a transverse displacement of the bunch. Because a spatial translation contributes only a phase factor to the Fourier transform, the magnitude of the bunch form factor, and therefore the CTR intensity, is largely unchanged by this displacement.

The contribution of this work is therefore not a new theory of CTR but a unification, pedagogically and computationally, of treatments that already exist in the literature in scattered form. Analytical CTR results have been derived for ellipsoidal, helically microbunched, and hollow Bessel electron beams, for finite and tilted radiators, and for particle-in-cell (PIC)-coupled in situ diagnostics. We have re-derived these in a common notation, embedded them in a single open implementation, and used that implementation to study an Airy-distributed bunch — a case that, to our knowledge, has not previously been treated in the CTR literature. The Airy result is the most immediate scientific outcome: it identifies a class of structured electron bunches for which CTR intensity is robust against longitudinal observation drift, which is potentially useful as a stable broadband source but problematic as a longitudinal-position diagnostic. Several limitations of the present treatment are worth stating explicitly. The pipeline uses the Ginzburg–Frank far-field kernel; pre-wave-zone effects and finite-radiator diffraction enter only through the analytical correction in Section 3, rather than through a full vector-electromagnetic solution in the spirit of Shkvarunets and Fiorito. The form factor is evaluated from analytical distributions rather than from PIC macroparticle data, so space-charge-induced distortions of the bunch profile must be supplied externally. A hollow Gaussian bunch, in particular, will produce CTR with nontrivial vector structure that an intensity-only treatment cannot capture. Addressing each of these limitations represents a natural next step rather than a fundamental obstacle: the pipeline's array-based, distribution-agnostic structure was designed to be extended.

Looking forward, three directions are most immediate. First, coupling the pipeline to a PIC or tracking code would close the loop between bunch design and CTR observables, enabling forward-model studies of how realistic compression, transport, and space-charge effects modify the form factor of an intended structured bunch. Second, integrating phase-sensitive observables — interferometric CTR or coherent heterodyne detection — would lift the intensity-only blind spot. Third, the framework as presented supports the design of CTR-based broadband sources in regimes — multi-octave, structured, polarization-engineered — that have been theorized but not yet experimentally realized; using $|f(k)|^2$ as a design variable rather than a measurement output is a natural next step toward generalized superradiance. More broadly, we hope this work establishes a habit of treating CTR not as a collection of geometry-specific special cases but as a single form-factor framework through which structured charge becomes structured light.

Bibliography

[1] Chad Pennington, Gia Azcoitia, Blae Stacey, Willi Kuropka, Jackson Rozells, Francois Lemery, Florian Burkart, and Sergio Carbajo. Optical superradiance from single-digit-femtosecond electron beam structure. 2026.

[2] V. L. Ginzburg and I. M. Frank. Radiation of a uniformly moving electron due to its transition from one medium to another. *Journal of Physics (USSR)*, 9:353–362, 1945.

[3] I. M. Frank. Transition radiation and the cherenkov effect. *Soviet Physics Uspekhi*, 4(5):740–746, 1962.

[4] G. M. Garibian. Contribution to the theory of transition radiation. *Soviet Physics JETP*, 6(6):1079–1088, 1958.

[5] G. M. Garibyan. Contribution to the theory of formation of transition x-radiation in a stack of plates. *Soviet Physics JETP*, 33(1):23–29, July 1971. Translated from Zhurnal Eksperimental'noi i Teoreticheskoi Fiziki, Vol. 60, pp. 39–52.

[6] M. Goldsmith and J. V. Jelley. Optical transition radiation from high-energy particles. *Philosophical Magazine*, 4(44):836–844, 1959.

[7] Y. Shibata, K. Ishi, T. Takahashi, T. Kanai, M. Ikezawa, K. Takami, T. Matsuyama, K. Kobayashi, and Y. Fujita. Observation of coherent transition radiation at millimeter and submillimeter wavelengths. *Phys. Rev. A*, 45:R8340–R8343, Jun 1992.

[8] Hung-chi Lihn, Pamela Kung, Chitrlada Settakorn, Helmut Wiedemann, David Bocek, and Michael Hernandez. Observation of stimulated transition radiation. *Phys. Rev. Lett.*, 76:4163–4166, May 1996.

[9] Sergio Carbajo. Structured photonics in light-matter interactions, accelerators, and x-ray lasers. In *2021 IEEE Photonics Conference (IPC)*, pages 1–2, 2021.

[10] Jingyi Tang, Randy Lemons, Wei Liu, Sharon Vetter, Timothy Maxwell, Franz-Josef Decker, Alberto Lutman, Jacek Krzywinski, Gabriel Marcus, Stefan Moeller, Zhirong Huang, Daniel Ratner, and Sergio Carbajo. Laguerre-gaussian mode laser heater for microbunching instability suppression in free-electron lasers. *Phys. Rev. Lett.*, 124:134801, Mar 2020.

[11] I. Nozawa, K. Kan, J. Yang, A. Ogata, T. Kondoh, M. Gohdo, K. Norizawa, H. Kobayashi, H. Shibata, S. Gonda, and Y. Yoshida. Measurement of $lt;20$ fs bunch length using coherent transition radiation. *Phys. Rev. ST Accel. Beams*, 17:072803, Jul 2014.

[12] R. Lai and A. J. Sievers. Determination of bunch asymmetry from coherent radiation in the frequency domain. *AIP Conference Proceedings*, 367(1):312–326, 04 1996.

[13] C.S. Thongbai and T. Vilaithong. Coherent transition radiation from short electron bunches. *Nuclear Instruments and Methods in Physics Research Section A: Accelerators, Spectrometers, Detectors and Associated Equipment*, 581(3):874–881, 2007.

[14] Bernhard Schmidt, Nils Maris Lockmann, Peter Schmüser, and Stephan Wesch. Benchmarking coherent radiation spectroscopy as a tool for high-resolution bunch shape reconstruction at free-electron lasers. *Phys. Rev. Accel. Beams*, 23:062801, Jun 2020.

[15] Matthias C. Hoffmann, Sebastian Schulz, Stephan Wesch, Steffen Wunderlich, Andrea Cavalleri, and Bernhard Schmidt. Coherent single-cycle pulses with mv/cm field strengths from a relativistic transition radiation light source. *Opt. Lett.*, 36(23):4473–4475, Dec 2011.

[16] Sergio Carbajo Garcia. Enabling technologies and applications of strong-field THz radiation in ultrafast and nonequilibrium dynamics. In Manijeh Razeghi and Mona Jarrahi, editors, *Terahertz Emitters, Receivers, and Applications XIV*, volume PC12683, page PC1268308. International Society for Optics and Photonics, SPIE, 2023.

[17] Dan Daranciang, John Goodfellow, Matthias Fuchs, Haidan Wen, Shambhu Ghimire, David A. Reis, Henrik Loos, Alan S. Fisher, and Aaron M. Lindenberg. Single-cycle terahertz pulses with >0.2v/Å field amplitudes via coherent transition radiation. *Applied Physics Letters*, 99(14):141117, 10 2011.

[18] J. Vieira, M. Pardal, J. T. Mendonça, et al. Generalized superradiance for producing broadband coherent radiation with transversely modulated arbitrarily diluted bunches. *Nature Physics*, 17:99–104, 2021.

[19] A. Gover. Superradiant and stimulated-superradiant emission in prebunched electron-beam radiators. *Physical Review Special Topics - Accelerators and Beams*, 8:030701, 2005.

[20] M. L. Ter-Mikaelian. *High-Energy Electromagnetic Processes in Condensed Media*, volume 29 of *Interscience Tracts on Physics and Astronomy*. Wiley-Interscience, New York, 1972.

[21] M. Castellano, V. Verzilov, L. Catani, A. Cianchi, G. D'Auria, M. Ferianis, and C. Rossi. Search for the prewave zone effect in transition radiation. *Physical Review E*, 67(1):015501, January 2003.

[22] Sara Casalbuoni, Bernhard Schmidt, and Peter Schmüser. Far-infrared transition and diffraction radiation: Part i: Production, diffraction effects and optical propagation. TESLA Report 2005-15, DESY, Hamburg, Germany, 2005.

[23] Siriwan Pakluea, Sakhorn Rimjaem, Jatuporn Saisut, and Chitrlada Thongbai. Coherent THz transition radiation for polarization imaging experiments. *Nuclear Instruments and Methods in Physics Research Section B: Beam Interactions with Materials and Atoms*, 464:28–31, 2020.

[24] S Casalbuoni, B Schmidt, P Schmüser, and B Steffen. Far-infrared transition and diffraction radiation. II. Technical report, DESY, Hamburg, 2006.

[25] U. Happek, A. J. Sievers, and E. B. Blum. Observation of coherent transition radiation. *Phys. Rev. Lett.*, 67:2962–2965, Nov 1991.

[26] Maxim V. Tsarev and Peter Baum. Characterization of non-relativistic attosecond electron pulses by transition radiation from tilted surfaces. *New Journal of Physics*, 20(3):033002, 2018.

[27] P. D. Hermes, R. Bruce, R. De Maria, M. Giovannozzi, A. Mereghetti, D. Mirarchi, S. Redaelli, and G. Stancari. Hl-lhc beam dynamics with hollow electron lenses. In *Proceedings of the 64th Advanced Beam Dynamics Workshop on High-Intensity and High-Brightness Hadron Beams (HB'21)*, pages 59–64, Geneva, Switzerland, 2024. JACoW Publishing.

[28] Noa Voloch-Bloch, Yossi Lereah, Yigal Lilach, Avraham Gover, and Ady Arie. Generation of electron airy beams. *Nature*, 494:331–335, 2013.

[29] G. A. Siviloglou, J. Broky, A. Dogariu, and D. N. Christodoulides. Observation of accelerating airy beams. *Phys. Rev. Lett.*, 99:213901, Nov 2007.